LhARA: The Laser-hybrid Accelerator for Radiobiological Applications

G. Aymar [1], **T. Becker** [2], **S. Boogert** [3], **M. Borghesi** [4], **R. Bingham** [5,1], **C. Brenner** [1], **P.N. Burrows** [6], **O.C. Ettlinger** [7], **T. Dascalu** [8], **S. Gibson** [3], **T. Greenshaw** [9], **S. Gruber** [10], **D. Gujral** [11], **C. Hardiman** [11], **J. Hughes** [9], **W.G. Jones** [8,21], **K. Kirkby** [13], **A. Kurup** [8], **J-B. Lagrange** [1], **K. Long** [8,1], **W. Luk** [8], **J. Matheson** [1], **P. McKenna** [5,15], **R. McLauchlan** [11], **Z. Najmudin** [7], **H.T. Lau** [8], **J.L. Parsons** [12,22], **J. Pasternak** [8,1], **J. Pozimski** [8,1], **K. Prise** [23], **M. Puchalska** [14], **P. Ratoff** [24,15], **G. Schettino**[16,20], **W. Shields** [3], **S. Smith** [17], **J. Thomason** [1], **S. Towe** [18], **P. Weightman** [8], **C. Whyte** [5], **R. Xiao** [19]

[1] *Science and Technology Facilities Council (STFC) Rutherford Appleton Laboratory, Harwell Campus, Didcot, OX11 0QX, UK*
[2] *Maxeler Technologies Limited, 3 Hammersmith Grove, London W6 0ND, UK*
[3] *John Adams Institute for Accelerator Science, Royal Holloway, University of London, Egham, Surrey, TW20 0EX, UK*
[4] *Centre for Plasma Physics, Department of Physics, Queens University Belfast, University Road, Belfast, BT7 1NN, Northern Ireland, UK*
[5] *Department of Physics, SUPA, University of Strathclyde, 16 Richmond Street, Glasgow, G1 1XQ, UK*
[6] *John Adams Institute for Accelerator Science, University of Oxford, Denys Wilkinson Building, Keble Road, Oxford OX1 3RH, UK*
[7] *John Adams Institute for Accelerator Science, Imperial College London, Exhibition Road, London, SW7 2AZ, UK*
[8] *Department of Physics, Imperial College London, Exhibition Road, London, SW7 2AZ, UK*
[9] *Department of Physics, University of Liverpool, Liverpool L3 9TA, UK*
[10] *Christian Doppler Laboratory for Medical Radiation Research for Radiation Oncology, Medical University of Vienna, Spitalgasse 23, 1090 Vienna, Austria*
[11] *Imperial College Healthcare NHS Trust, The Bays, South Wharf Road, St Mary's Hospital, London W2 1NY, UK*
[12] *Institute of Translational Medicine, Department of Molecular and Clinical Cancer Medicine, University of Liverpool, Liverpool L3 9TA, UK*
[13] *Division of Cancer Sciences, School of Medical Sciences, University of Manchester, Oxford Road, Manchester, M13 9PL, UK*
[14] *Technische Universität Wien, Atominstitut, Stadionallee 2, 1020 Vienna, Austria*
[15] *Cockcroft Institute, Daresbury Laboratory, Sci-Tech Daresbury, Daresbury, Warrington, WA4 4AD, UK*
[16] *National Physical Laboratory, Hampton Road, Teddington, Middlesex, TW11 0LW, UK*
[17] *STFC Daresbury Laboratory, Daresbury, Cheshire, WA4 4AD, UK*
[18] *Leo Cancer Care, Broadview, Windmill Hill, Hailsham, East Sussex, BN27 4RY, UK*
[19] *Corerain Technologies, 14F, Changfu Jinmao Building (CFC), Trade-free Zone, Futian District, Shenzhen, Guangdong, China*
[20] *University of Surrey, 388 Stag Hill, Guilford, GU2 7XH, UK*
[21] *Imperial Patient and Public Involvement Group (IPPIG), Imperial College London, Exhibition Road, London, SW7 2AZ, UK*

ABSTRACT

The 'Laser-hybrid Accelerator for Radiobiological Applications', LhARA, is conceived as a novel, flexible facility dedicated to the study of radiobiology. The technologies demonstrated in LhARA, which have wide application, will be developed to allow particle-beam therapy to be delivered in a new regimen, combining a variety of ion species in a single treatment fraction and exploiting ultra-high dose rates. LhARA will be a hybrid accelerator system in which laser interactions drive the creation of a large flux of protons or light ions that are captured using a plasma (Gabor) lens and formed into a beam. The laser-driven source allows protons and ions to be captured at energies significantly above those that pertain in conventional facilities, thus evading the current space-charge limit on the instantaneous dose rate that can be delivered. The laser-hybrid approach, therefore, will allow the radiobiology that determines the response of tissue to ionising radiation to be studied with protons and light ions using a wide variety of time structures, spectral distributions, and spatial configurations at instantaneous dose rates up to and significantly beyond the ultra-high dose-rate 'FLASH' regime.

It is proposed that LhARA be developed in two stages. In the first stage, a programme of *in vitro* radiobiology will be served with proton beams with energies between 10 MeV and 15 MeV. In stage two, the beam will be accelerated using a fixed-field alternating-gradient accelerator (FFA). This will allow experiments to be carried out *in vitro* and *in vivo* with proton beam energies of up to 127 MeV. In addition, ion beams with energies up to 33.4 MeV per nucleon will be available for *in vitro* and *in vivo* experiments. This paper presents the conceptual design for LhARA and the R&D programme by which the LhARA consortium seeks to establish the facility.

LAY SUMMARY

It is well established that radiation therapy (RT) is an effective treatment for many types of cancer. Most treatments are delivered by machines that accelerate electrons which are then used to produce a beam of high-energy photons (X-rays) which are directed at a tumour to kill cancer cells. However, healthy tissue anywhere in the path of the photon beam is also irradiated and so can be damaged. Modern X-ray therapy is able to reduce this damage by using several beams at different angles.

Recent years have seen the use of a new type of machine in which protons are accelerated to produce proton beams (rather than photon beams) which are directed at a tumour. These proton beams can be arranged to deposit almost all of their energy in a small volume within a tumour so they cause little damage to healthy tissue; a major advantage over photon beams. But proton machines are large and expensive, so there is a need for the development of proton machines that are smaller, cheaper and more flexible in how they can be used.

The LhARA project is aimed at the development of such proton machines using a new approach based on high power lasers. Such new machines could also make it easier to deliver the dose in very short high-intensity pulses and as a group of micro-beams—exciting recent research has shown that this brings improved effectiveness in killing cancer cells while sparing healthy tissue. The technology to be proved in LhARA should enable a course of RT to be delivered in days rather than weeks.

Scientifically, there is a need to understand better the basic processes by which radiation interacts with biological matter to kill cancer cells—the investigation of these processes involves physics as well as biology. Thus the most important aim of LhARA is to pursue this radiobiological

research in new regimens and from this to develop better treatments. LhARA will also pursue technological research into laser-hybrid accelerators.

Keywords: Radiobiology, Novel acceleration, Proton beam therapy, Ion beam therapy, Laser-driven acceleration, Plasma lens, Fixed-field alternating-gradient acceleration

1 INTRODUCTION

Cancer is the second most common cause of death globally [The World Health Organisation (2020)]. In 2018, 18.1 million new cancer cases were diagnosed, 9.6 million people died of cancer-related disease, and 43.8 million people were living with cancer [Bray et al. (2018); Fitzmaurice et al. (2018)]. It is estimated that 26.9 million life-years could be saved in low- and middle-income countries if radiotherapy capacity could be scaled up [Atun et al. (2015)]. Novel techniques incorporated in facilities that are at once robust, automated, efficient, and cost-effective are required to deliver the required scale-up in provision.

Radiation therapy, a cornerstone of cancer treatment, is used in over 50 % of cancer patients [Datta et al. (2019)]. The most frequently used types of RT employ photon or electron beams with MeV-scale energies. Proton and ion beams offer substantial advantages over X-rays because the bulk of the beam energy is deposited in the Bragg peak. This allows dose to be conformed to the tumour while sparing healthy tissue and organs at risk. The benefits of proton and ion-beam therapy (PBT) are widely recognised. PBT today is routinely delivered in fractions of ~ 2 Gy per day over several weeks; each fraction being delivered at a rate of $\lesssim 5$ Gy/minute deposited uniformly over the target treatment volume. There is evidence of therapeutic benefit when dose is delivered at ultra-high rate, $\gtrsim 40$ Gy/s, in "FLASH" RT [Berry (1973); Favaudon et al. (2014); Durante et al. (2018); Vozenin et al. (2019); Wilson et al. (2020b)] or when multiple micro-beams with diameter less than 1 mm distributed over a grid with inter-beam spacing ~ 3 mm are used [Prezado and Fois (2013); Prezado et al. (2017b,a, 2018); González and Prezado (2018); Martínez-Rovira et al. (2017)]. However, the radiobiological mechanisms by which the therapeutic benefit is generated using these approaches are not entirely understood.

LhARA, the Laser-hybrid Accelerator for Radiobiological Applications, is conceived as the new, highly flexible, source of radiation that is required to explore the mechanisms by which the biological response to ionising radiation is determined by the physical characteristics of the beam. A high-power pulsed laser will be used to drive the creation of a large flux of protons or ions which are captured and formed into a beam by strong-focusing plasma lenses. The plasma (Gabor) lenses provide the same focusing strength as high-field solenoids at a fraction of the cost. Rapid acceleration will be performed using a fixed-field alternating-gradient accelerator (FFA), thereby preserving the unique flexibility in the time, energy, and spatial structure of the beam afforded by the laser-driven source.

The LhARA facility may be developed in two stages. In the first stage, the laser-driven beam, captured and transported using plasma lenses and bending magnets, will serve a programme of *in vitro* radiobiology with proton beams of energy of up to 15 MeV. In stage two, the beam will be accelerated using an FFA. This will allow experiments to be carried out *in vitro* and *in vivo* with proton-beam energies of up to 127 MeV. Ion beams (including C^{6+}) with energies up to 33.4 MeV per nucleon will also be available.

The laser pulse that initiates the production of protons or ions at LhARA may be triggered at a repetition rate of up to 10 Hz. The time structure of the beam may therefore be varied to interrupt the chemical and biological pathways that determine the biological response to ionising radiation using 10 ns to 40 ns long proton or ion bunches repeated at intervals as small as 100 ms. The technologies chosen to capture, transport, and accelerate the beam in LhARA ensure that this unique capability is preserved. The LhARA beam may be used to deliver an almost uniform dose distribution over a circular area with a maximum diameter of between 1 cm and 3 cm. Alternatively, the beam can be focused to a spot with diameter of ~ 1 mm.

The technologies that will be developed in LhARA have the potential to make PBT available to the many. The laser-hybrid approach will allow radiobiological studies and eventually radiotherapy to be carried out

in completely new regimens, delivering a variety of ion species in a broad range of time structures, spectral distributions, and spatial configurations at instantaneous dose rates up to and potentially significantly beyond the current ultra-high dose-rate "FLASH" regime.

The "pre Conceptual Design Report" (pre-CDR) for LhARA [The LhARA consortium (2020)] lays the foundations for the development of full conceptual and technical designs for the facility. The pre-CDR also contains a description of the R&D that is required to demonstrate the feasibility of critical LhARA components and systems. This paper presents a summary of the contents of the pre-CDR and lays out the vision of the LhARA consortium.

2 MOTIVATION

RT delivered using protons and ions, PBT, has the potential to overcome some of the fundamental limitations of X-rays in cancer treatment through the targeted delivery of the radiation dose [Loeffler and Durante (2013)]. The Particle Therapy Co-Operative Group (PTCOG) currently lists 90 proton therapy facilities and 12 carbon ion therapy facilities worldwide, located predominantly in high-income countries [PTCOG (2020)]. Low- and middle-income countries (LMIC) are relatively poorly served, indeed nearly 70% of cancer patients globally do not have access to RT [Datta et al. (2019)].

The case for a systematic study of the radiobiology of proton and ion beams

The efficacy of proton and ion beams is characterised by their relative biological effectiveness (RBE) in comparison to a reference photon beam. The treatment-planning software that is in use in the clinic today assumes an RBE value for protons of 1.1 [Paganetti and van Luijk (2013)], meaning that, compared to X-rays, a lower dose of protons is needed to produce the same therapeutic effect. However, the rapid rise in the linear energy transfer (LET) at the Bragg peak leads to significant uncertainties in the RBE. Furthermore, it is known that RBE depends strongly on many factors, including particle energy, dose, dose rate, the degree of hypoxia, and tissue type [Paganetti (2014)]. Indeed, RBE values from 1.1 to over 3 have been derived from *in vitro* clonogenic-survival assay data following proton irradiation of cultured cell lines derived from different tumours [Paganetti (2014); Chaudhary et al. (2014); Wilkens and Oelfke (2004)]. RBE values of ~ 3 are accepted for high-LET carbon-ion irradiation, although higher values have been reported [Karger and Peschke (2017)]. RBE uncertainties for carbon and other ion species are at least as large as they are for protons. These uncertainties can lead to an incorrect estimation of the dose required to treat a particular tumour. Overestimation can lead to the damage of healthy tissue, while an underestimate can lead to the tumour not being treated sufficiently for it to be eradicated.

The radiotherapeutic effect is caused largely by irreparable damage to the cell's DNA. The spectrum of DNA damage induced within tumour cells changes in response to differences in RBE. Larger RBE values, corresponding to higher LET, can increase the frequency and complexity of DNA damage, in particular causing DNA double-strand breaks (DSB) and complex DNA damage (CDD), where multiple DNA lesions are induced in close proximity [Vitti and Parsons (2019); Carter et al. (2018)]. These DNA lesions are a major contributor to radiation-induced cell death as they represent a significant barrier to the cellular DNA-repair machinery [Vitti and Parsons (2019)]. However, a number of other biological factors contribute to varying RBE in specific tumours, including the intrinsic radio-sensitivity of the tissue, the level of oxygenation (hypoxia), the growth and re-population characteristics, and the associated tumour micro-environment. Consequently, there is still significant uncertainty in the precise radiobiological mechanisms that arise and how these mechanisms determine the impact of PBT. Detailed systematic studies of the biophysical effects of the interaction of protons and ions, under different physical conditions, with different

tissue types will provide important information on RBE variation and could enable enhanced patient treatment-planning algorithms to be devised. In addition, studies examining the impact of combination therapies with PBT (e.g. targeting the DNA damage response, hypoxia signalling mechanisms and also the tumour micro-environment) are currently sparse; performing these studies will therefore provide input vital to the development of future personalised patient-therapy strategies using PBT.

The case for novel beams for radiobiology

Extending the range of beam characteristics used in PBT delivery may have significant therapeutic benefits. Delivery of RT at high dose rates has led to noticeably reduced lung fibrosis in mice, reduced skin toxicity in mini-pigs, and reduced side-effects in cats with nasal squamous-cell carcinoma, effects currently thought to be mediated via local oxygen depletion [Wilson et al. (2020b,a)]. In fact, the first patient with CD30+ T-cell cutaneous lymphoma has been safely treated with electrons delivered at FLASH dose rates [Bourhis et al. (2019)]. In addition, therapeutic benefit has been demonstrated with the use of multiple micro-beams [Prezado et al. (2017b)]. However, there is still significant uncertainty regarding the thresholds and the radiobiological mechanisms underlying these effects. Extensive further study both *in vitro* and in appropriate *in vivo* models is required.

The LhARA facility will provide access to proton and stable ion beams, provide a wide variety of temporal, spatial, and spectral fractionation schemes, and deliver reliable and reproducible biological data with fewer constraints than at current clinical centres. LhARA will allow direct radiobiological comparisons of the effects of different charged particles at different energies and dose rates and enable unique mechanistic studies (e.g. examination of the oxygen depletion hypothesis for FLASH). In addition, LhARA will enable exhaustive evaluations of RBE using more complex end-points (e.g. angiogenesis and inflammation) in addition to routine survival measurements. The ability to evaluate charged particles in conjunction with other therapies (immunotherapy and chemotherapy) and to perform *in vivo* experiments with the appropriate animal models is of great importance given the current lack of evidence in these areas. LhARA therefore has the potential to provide the radiobiological data required to improve clinical practice.

The simulations of LhARA presented in this document have been used to estimate the dose delivered as a function of energy for protons and carbon ions. These simulations, described in sections 3.3 and 3.4, show instantaneous particle rates of the order of 10^9 particles per shot can be achieved, corresponding to average dose rates of up to $\gtrsim 120\,\mathrm{Gy/s}$ for protons and $\gtrsim 700\,\mathrm{Gy/s}$ for carbon ions. These estimates are based on the baseline specifications for LhARA.

Laser-hybrid beams for radiobiology and clinical application

High-power lasers have previously been proposed as an alternative to conventional proton and carbon-ion facilities for radiotherapy [Bulanov et al. (2002); Fourkal et al. (2003); Malka et al. (2004); Ledingham et al. (2003)]. Laser-driven sources have also been proposed as the basis for electron, proton and ion-beams for radiobiology [Kraft et al. (2010); Fiorini et al. (2011); Yogo et al. (2011); Bin et al. (2012); Doria et al. (2012); Zeil et al. (2013); Masood et al. (2014); Zlobinskaya et al. (2014)]. While a number of cell irradiation experiments have been conducted with laser-accelerated ions [Doria et al. (2012); Zeil et al. (2013); Pommarel et al. (2017); Manti et al. (2017)], these have been limited in scope to a single-shot configuration. More recent projects (e.g. A-SAIL [A-SAIL Project (2020)], ELI [Cirrone et al. (2013)] and SCAPA [Wiggins et al. (2019)]) will also investigate radiobiological effects using laser-driven ion beams. These studies will also address various technological issues [Manti et al. (2017); Romano et al. (2016a); Masood et al. (2017); Chaudhary et al. (2017); Margarone et al. (2018)].

A beam line to provide ion-driven beams for multi-disciplinary applications, ELIMAIA (ELI Multidisciplinary Applications of laser-Ion Acceleration) is being brought into operation at the Extreme Light Infrastructure (ELI) [Cirrone et al. (2020); Schillaci et al. (2019)]. This beam line will include the "ELI MEDical and multidisciplinary applications" (ELIMED) beam line which will allow radiobiological investigations to be carried out [Cirrone et al. (2016); Romano et al. (2016b); Milluzzo et al. (2017); Pipek et al. (2017); Milluzzo et al. (2018); Cirrone et al. (2020)]. LhARA is distinguished from this facility in that the energy at which the beam will be captured has been chosen to maximise the shot-to-shot stability of the particle flux.

Protons and ions at conventional facilities are captured at energies of several tens of keV. At such low energies, the mutual repulsion of the particles, the "space-charge effect", limits the maximum instantaneous dose rate. The laser-driven source allows protons and ions to be captured at significantly higher energies, thus evading the current space-charge limit. Rapid acceleration will be performed using a fixed-field alternating-gradient accelerator (FFA), thereby preserving the unique flexibility in the time, energy, and spatial structure of the beam afforded by the laser-driven source. Modern lasers are capable of delivering a Joule of energy in pulses that are tens of femtoseconds in length at repetition rates of $\gtrsim 10$ Hz. Laser-driven ion sources create beams that are highly divergent, have a large energy spread, and an intensity that can vary by up to 25% pulse-to-pulse [Dover et al. (2020)]. These issues are addressed in the LhARA conceptual design through the use of Gabor lenses to provide strong focusing and to allow energy selection. In addition, sophisticated instrumentation will be used in a fast feedback-and-control system to ensure that the dose delivered is both accurate and reproducible. This approach will allow multiple ion species, from proton to carbon, to be produced from a single laser by varying the target foil and particle-capture optics.

LhARA will prove the principle of the novel technologies required for the development of future therapy facilities. The legacy of the LhARA programme will therefore be: a unique facility dedicated to the development of a deep understanding of the radiobiology of proton and ion beams; and the demonstration in operation of technologies that will allow PBT to be delivered in completely new regimens.

3 THE LHARA FACILITY

The LhARA facility, shown schematically in figure 1, has been designed to serve two end stations for *in vitro* radiobiology and one end station for *in vivo* studies. The principle components of Stage 1 of the LhARA accelerator are: the laser-driven proton and ion source; the matching and energy selection section; beam delivery to the low-energy *in vitro* end station; and the low-energy abort line. Stage 2 is formed by the injection line for the fixed-field alternating-gradient accelerator (FFA); the FFA; the extraction line; the high-energy abort line; beam delivery to the high-energy *in vitro* end station; and the transfer line to the *in vivo* end station. Proton beams with energies of between 10 MeV and 15 MeV will be delivered directly from the laser-driven source to the low-energy *in vitro* end station via a transfer line. The high-energy *in vitro* end station and the *in vivo* end station will be served by proton beams with energy between 15 MeV and 127 MeV and by ion beams, including C^{6+} with energies up to 33.4 MeV/u. The design parameters for the various components of LhARA are given in tables 1 and 2. The design of the LhARA facility is described in the sections that follow.

3.1 Laser-driven proton and ion source

A novel solution for proton and ion acceleration is to use a compact, flexible laser-driven source coupled to a state-of-the-art beam-transport line. This allows an accelerating gradient of $\gtrsim 10$ GV/m to be exploited

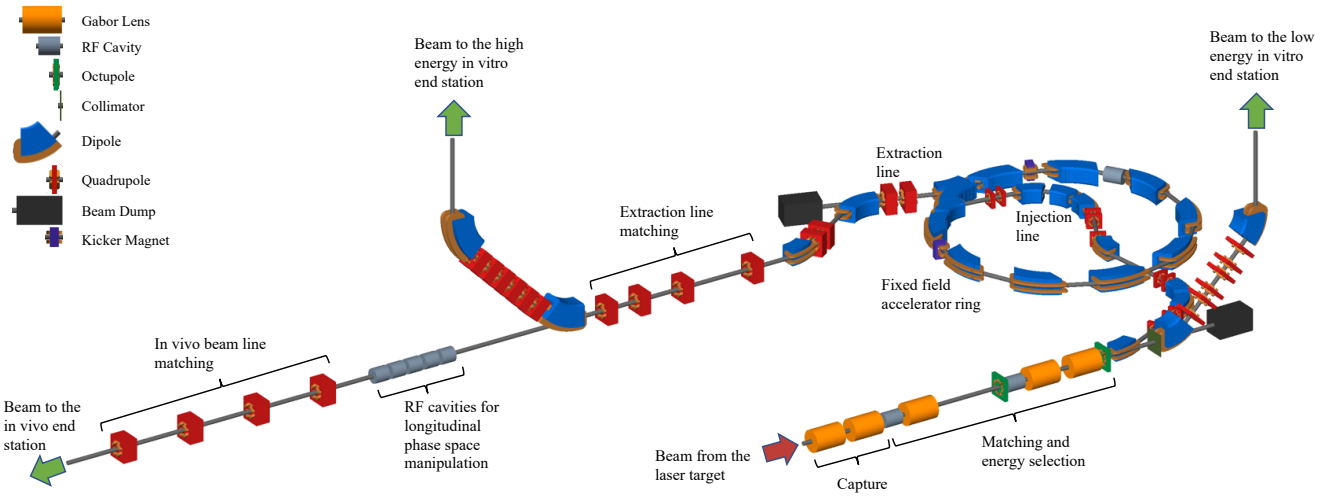

Figure 1. Schematic diagram of the LhARA beam lines. The particle flux from the laser-driven source is shown by the red arrow. The 'Capture' section is followed by the 'Matching and energy selection' sections, the beam is directed either into the 90° bend that takes it to the low-energy *in vitro* end station, towards the FFA injection line, or to the low-energy beam dump. Post acceleration is performed using the FFA, on extraction from which the beam is directed either to the high-energy *in vitro* end station, the *in vivo* end station, or the high-energy beam dump. Gabor lenses are shown as orange cylinders, RF cavities as grey cylinders, octupole magnets as green discs, collimators as dark-green bars, dipole magnets are shown in blue, quadrupole magnets are shown in red, beam dumps (black rectangles) and kicker magnets are also shown.

at the laser-driven source. We propose to operate in the laser-driven sheath-acceleration regime [Clark et al. (2000a); Snavely et al. (2000); Daido et al. (2012); Roth and Schollmeier (2016)] for ion generation. An intense, short laser pulse will be focused onto a target. The intense electric field generated on the front surface of the target accelerates the surface electrons, driving them into the material. Electrons which gain sufficient energy traverse the target, ionising the material as they go. A strong space-charge electric field, the 'sheath', is created as the accelerated electrons exit the rear surface of the target. This field in turn accelerates protons and ions present as contaminants on the surface. The sheath-acceleration scheme has been shown to produce ion energies greater than 40 MeV/u at the highest laser intensities [Dover et al. (2020)]. The maximum proton energy (E_p) scales with laser intensity (I) as, $E_p \propto I^{\frac{1}{2}}$. The laser required to deliver a significant proton flux at 15 MeV is commercially available.

The distribution of proton and ion energies observed in laser-driven beams exhibits a sharp cut-off at the maximum energy and, historically, the flux of laser-accelerated ion beams has varied significantly shot-to-shot. To reduce these variations, the choice has been made to select particles from the plateau of the two-temperature energy spectrum of the laser-accelerated ion beam [Clark et al. (2000b); Passoni et al. (2010)]. This should enhance ion-beam stability and allow reproducible measurements to be carried out at ultra-high dose rates using a small number of fractions. To create the flux required in the plateau region, it is proposed that a 100 TW laser system is used. A number of commercial lasers are available that are capable of delivering $> 2.5\,\mathrm{J}$ in pulses of duration $< 25\,\mathrm{fs}$, at 10 Hz with contrast better than $10^{10} : 1$. Shot-to-shot stability of $< 1\%$ is promised, an important feature for stable ion-beam production.

Target

Key to the operation of this configuration is a system that refreshes the target material at high repetition-rate

Table 1. Design parameters of the components of the LhARA facility. The parameter table is provided in a number of sections. This section contains parameters for the Laser-driven proton and ion source, the Proton and ion capture section, and the Stage 1 beam transport section.

Parameter	Value or range	Unit
Laser driven proton and ion source		
Laser power	100	TW
Laser Energy	2.5	J
Laser pulse length	25	fs
Laser rep. rate	10	Hz
Required maximum proton energy	15	MeV
Proton and ion capture		
Beam divergence to be captured	50	mrad
Gabor lens effective length	0.857	m
Gabor lens length (end-flange to end-flange)	1.157	m
Gabor lens cathode radius	0.0365	m
Gabor lens maximum voltage	65	kV
Number of Gabor lenses	2	
Alternative technology: solenoid length	1.157	m
Alternative technology: solenoid max field strength	1.3	T
Stage 1 beam transport: matching & energy selection, beam delivery to low-energy end station		
Number of Gabor lenses	3	
Number of re–bunching cavities	2	
Number of collimators for energy selection	1	
Arc bending angle	90	Degrees
Number of bending magnets	2	
Number of quadrupoles in the arc	6	
Alternative technology: solenoid length	1.157	m
Alternative technology: solenoid max field strength (to serve the injection line to the Stage 2)	0.8 (1.4)	T

in a reproducible manner. A number of schemes have been proposed for such studies, including high-pressure gases [Willingale et al. (2009); Bin et al. (2015); Chen et al. (2017)], cryogenic hydrogen ribbons [Margarone et al. (2016); Gauthier et al. (2017); Obst et al. (2017)], liquid sheets [Morrison et al. (2018)] and tape drives [Noaman-ul Haq et al. (2017)]. For LhARA, a tape drive based on the system developed at Imperial College London is proposed [Dover et al. (2020)]. This system is capable of reliable operation at target thicknesses down to 5 μm, using aluminium or steel foils, and down to 18 μm using plastic tapes. Such tape-drive targets can be operated at high charge (up to 100 pC at 15 ± 1 MeV, i.e. $> 10^9$ protons per shot) and can deliver high-quality proton and ion fluxes at repetition rates of up to 10 Hz or greater.

The careful control of the tension of the tape in a tape-drive target is critical for reproducible operation. The tape must be stretched enough to flatten the surface, but not enough to cause plastic deformations. Surface flatness is important for a number of reasons. Rippling of the front surface modifies the laser absorption dramatically; uncharacterised rippling can make shot-to-shot variations significant and unpredictable [Noaman-ul Haq et al. (2017)]. Similarly, rear surface perturbations can modify the sheath field, resulting in spatial non-uniformities of the proton beam or suppression of the achievable peak energies. Tape drives with torsion control and monitoring to maintain a high-quality tape surface have been designed and operated in experiments at Imperial College London. The development of these targets continues with a view to the production of new, thinner tapes for improved ion generation and the creation of ion species

Table 2. Design parameters of the components of the LhARA facility. The parameter table is provided in a number of sections. This section contains parameters for the Stage 2 beam transport and the *in vitro* and *in vivo* end stations.

Parameter	**Value or range**	**Unit**
Stage 2 beam transport: FFA, transfer line, beam delivery to high-energy end stations		
Number of bending magnets in the injection line	7	
Number of quadrupoles in the injection line	10	
FFA: Machine type	single spiral scaling FFA	
FFA: Extraction energy	15–127	MeV
FFA: Number of cells	10	
FFA: Orbit $R_{\rm min}$	2.92	m
FFA: Orbit $R_{\rm max}$	3.48	m
FFA: Orbit excursion	0.56	m
FFA: External R	4	m
FFA: Number of RF cavities	2	
FFA: RF frequency	1.46–6.48	MHz
FFA: harmonic number	1, 2 or 4	
FFA: RF voltage (for 2 cavities)	4	kV
FFA: spiral angle	48.7	Degrees
FFA: Max B field	1.4	T
FFA: k	5.33	
FFA: Magnet packing factor	0.34	
FFA: Magnet opening angle	12.24	degrees
FFA: Magnet gap	0.047	m
FFA: Ring tune (x,y)	(2.83,1.22)	
FFA: γ_T	2.516	
FFA: Number of kickers	2	
FFA: Number of septa	2	
Number of bending magnets in the extraction line	2	
Number of quadrupoles in the extraction line	8	
Vertical arc bending angle	90	Degrees
Number of bending magnets in the vertical arc	2	
Number of quadrupoles in the vertical arc	6	
Number of cavities for longitudinal phase space manipulation	5	
Number of quadrupoles in the in vivo beam line	4	
***In vitro* biological end stations**		
Maximum input beam diameter	1-3	cm
Beam energy spread (full width)	Low-energy end station: ≤ 4 High-energy end station: ≤ 1	% %
Input beam uniformity	< 5	%
Scintillating fibre layer thickness	0.25	mm
Air gap length	5	mm
Cell culture plate thickness	1.3	mm
Cell layer thickness	0.03	mm
Number of end stations	2	
***In vivo* biological end station**		
Maximum input beam diameter	1-3	cm
Beam energy spread (full width)	≤ 1	%
Input beam uniformity	< 5	%
Beam options	Spot-scanning, passive scattering, micro-beam	

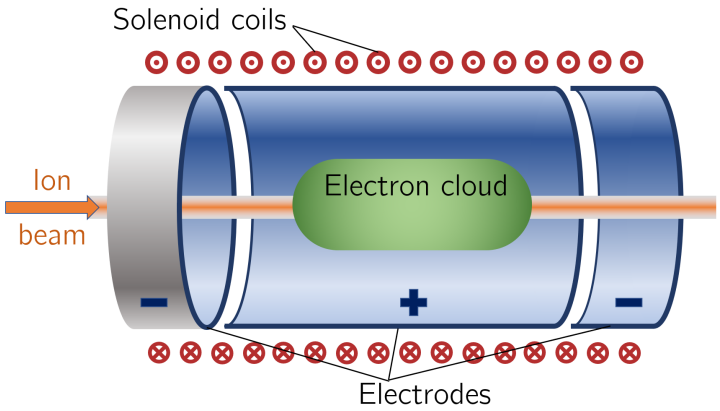

Figure 2. Schematic diagram of a Penning-Malmberg trap of the type proposed for use in the Gabor lenses to be used in LhARA. The solenoid coils, and the direction of current flow, are indicated by the red circles (the central dots indicate current emerging from the picture, crosses current entering it). The confining electrostatic potential is provided using a central cylindrical anode and two cylindrical negative end electrodes. The ion beam enters on-axis from the left and the electron cloud is indicated by the green shaded area.

other than protons and carbon. This is an active area of R&D that will continue with the development of LhARA.

3.2 Proton and ion capture

The use of an electron cloud as a focusing element for charged-particle beams was first proposed by Gabor [Gabor (1947)]. The electron cloud is confined within the lens using a long cylindrical anode placed within a uniform solenoid field, see figure 2. Such a configuration is commonly known as a 'Penning trap' and has found wide application in many fields [Thompson (2015)]. Variations on the Penning trap where axial apertures in the cathodes are introduced, such as the Penning-Malmberg trap [deGrassie and Malmberg (1980); Malmberg et al. (1988)] are attractive for beam-based applications due to the excellent access provided to the plasma column.

The focal length of a Gabor lens of length l is given in terms of the electron number density by:

$$\frac{1}{f} = \frac{e^2 n_e}{4\epsilon_0 U} l \,; \tag{1}$$

where e is the magnitude of the electric charge of the electron, n_e is the number density of the electrons confined within the lens, ϵ_0 the permittivity of free space, and U the kinetic energy of the particle beam. The desired focusing strength determines n_e which in turn allows the anode voltage and magnetic-field strength to be calculated [Reiser (1989); Pozimski and Aslaninejad (2013)]. The focal lengths required to capture the proton and ion beams at LhARA have been chosen such that the necessary electron number densities lie well within the range achieved in published experiments.

For a given focal length, the magnetic field strength required in the Gabor lens is smaller than that of a solenoid that would give equivalent focusing. In the non-relativistic approximation, the relationship between the magnetic field strength in the Gabor lens, B_{GBL}, and the equivalent solenoid, B_{sol}, is given

by [Pozimski and Aslaninejad (2013)]:

$$B_{\mathrm{GBL}} = B_{\mathrm{sol}}\sqrt{Z\frac{m_e}{m_p}}\,; \tag{2}$$

where Z is the charge state of the ions. In the case of a proton beam, the reduction factor is 43. This means the cost of the solenoid for a Gabor lens can be significantly lower than the cost of a solenoid of equivalent focusing strength.

Instability of the electron cloud is a concern in the experimental operation of a Gabor lens; azimuthal beam disruption due to the diocotron instability has been observed and described theoretically [Meusel et al. (2013)]. Theory indicates that the diocotron instability is most problematic under well-defined geometric conditions. The reliable operation of a Gabor lens in a regime free from this instability has yet to be demonstrated. Gabor lenses promise very strong focusing, simple construction, and low magnetic field, all attractive features for LhARA. However, these attractive features come at the cost of relatively high voltage operation ($\gtrsim 50\,\mathrm{kV}$) and possible vulnerability to instability.

With reliable operation of Gabor lenses as yet unproven, we plan a two-part experimental and theoretical programme of research to investigate their suitability. Initial work will include: the theoretical study of lens stability using a full 3D particle-in-cell code such as VSIM [TECH-X (2020)]; and the development of electron-density diagnostics based on interferometric measurement of the resulting refractive-index change. A test Gabor lens will be constructed to allow validation of both the simulation results and a new diagnostic tool using an alpha emitter as a proxy for the LhARA beam. In addition, the initial investigation will include the design of an injection system to fill the lens with the required electron cloud. Should it prove impossible to produce a suitable Gabor lens, it will be necessary to use high-field solenoids to produce the equivalent focusing effect.

3.3 Beam transport and delivery to the low-energy *in vitro* end station

The beam transport line to the low-energy *in vitro* end station must produce a uniform dose distribution at the cell layer. Beam losses must be minimised for radiation safety and to maximise the dose that can be delivered in a single shot. The transport line has been designed to minimise regions in which the beam is brought to a focus to reduce the impact of space-charge forces on the beam phase-space. An optical solution was initially developed using Beamoptics [Autin et al. (1998)] and MADX [Grote and Schmidt (2003)]. Accurate estimation of the performance of the beam line requires the inclusion of space-charge forces and particle-matter interactions. Performance estimation was therefore performed using Monte Carlo particle-tracking from the ion source to the end station. BDSIM [Nevay et al. (2020)], which is based on the GEANT4 toolkit, was used for the simulation of energy deposition arising from beam interactions with the material in the accelerator and the end station. GPT [De Loos and Van der Geer (1996)] was used for evaluating the full 3D impact of space-charge effects.

An idealised Gaussian beam was generated with a spot size of 4 μm FWHM, an angular divergence of 50 mrad, 35 fs FWHM bunch length, and an energy spread of 1×10^{-6} MeV. The maximum estimated bunch charge is 1×10^{9} protons. The presence of a substantial electron flux produced from the laser target compensates the high proton charge density in the vicinity of the ion-production point. To approximate the partial space-charge compensation in this region, it was assumed that co-propagating electrons would fully compensate the space-charge forces over the first 5 cm of beam propagation. Beyond this, the proton beam was assumed to have separated from the co-propagating electrons sufficiently for space-charge to become

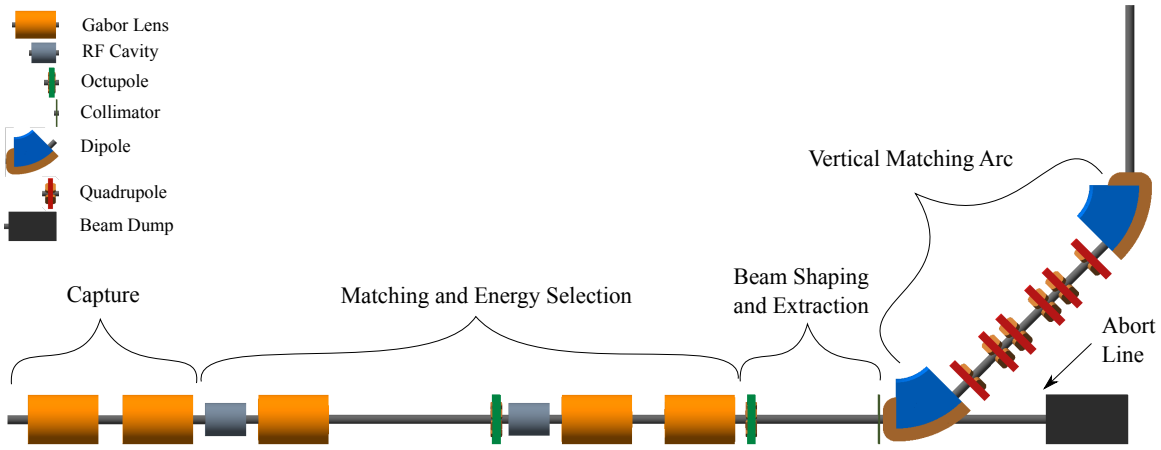

Figure 3. Beam transport for Stage 1 of LhARA visualised in BDSIM, showing five machine sections. The capture section is composed of two Gabor lenses (orange cylinders). The matching and energy selection section includes three Gabor lenses, two RF cavities (grey cylinders) and an octupole magnet (green disc). The beam shaping and extraction section includes a second octupole and a collimator (vertical dark-green bar). The vertical matching arc directs the beam into the low-energy *in vitro* end station and is composed of two 45° dipoles (blue and brown) and six quadrupoles (red). The total length of this beam line is 17.3 m.

a significant effect and cause emittance growth. Therefore, a further 5 cm drift was simulated including space-charge forces. At a distance of 10 cm from the ion source, the beam is at the exit of the laser-target vessel. The kinematic distributions of ions in the beam were stored at this point and passed to the relevant BDSIM and GPT simulations of the downstream beam line.

The Stage 1 beam line, shown schematically in figure 3, is composed of five sections: beam capture; matching and energy selection; beam shaping; vertical arc matching; and an abort line. The capture section uses two Gabor lenses to minimise the transverse momentum of particles in the beam. Beyond the capture section, an RF cavity permits control of the bunch length and manipulation of the longitudinal phase-space. A third Gabor lens then focuses the bunch to a small spot size after which a second RF cavity is located to provide further longitudinal phase-space manipulation. Two further Gabor lenses ensure the beam is again parallel before it enters the vertical 90° arc. All Gabor lenses have an inner radius of 3.65 cm and an effective length of 0.857 m. All lenses operate at a cathode voltage of less than 65 kV.

The parallel beam that emerges from the final Gabor lens, provides significant flexibility for the inclusion of beam shaping and extraction systems. Beam uniformity will be achieved using octupole magnets to provide third-order focusing to perturb the first-order focusing of the Gabor lenses. Such schemes have been demonstrated in magnetic lattices in a number of facilities [Tsoupas et al. (1991); Urakabe et al. (1999); Amin et al. (2018)]. A suitable position for the first octupole was identified to be after the final Gabor lens where the beam is large; its effect on the beam is expected to be significant. Octupoles were only modelled in BDSIM as GPT does not have a standard component with an octupolar field. The typical rectangular transverse distribution resulting from octupolar focusing requires collimation to match the circular aperture through which the beam enters the end station. A collimator is therefore positioned at the start of the vertical arc. Further simulations are required to determine the optimum position of the second octupole and to evaluate the performance of the octopoles. The switching dipole which directs the beam to the injection line of the FFA in Stage 2 will be located between the second octupole and the collimator, requiring the octupole to be ramped down for Stage 2 operation.

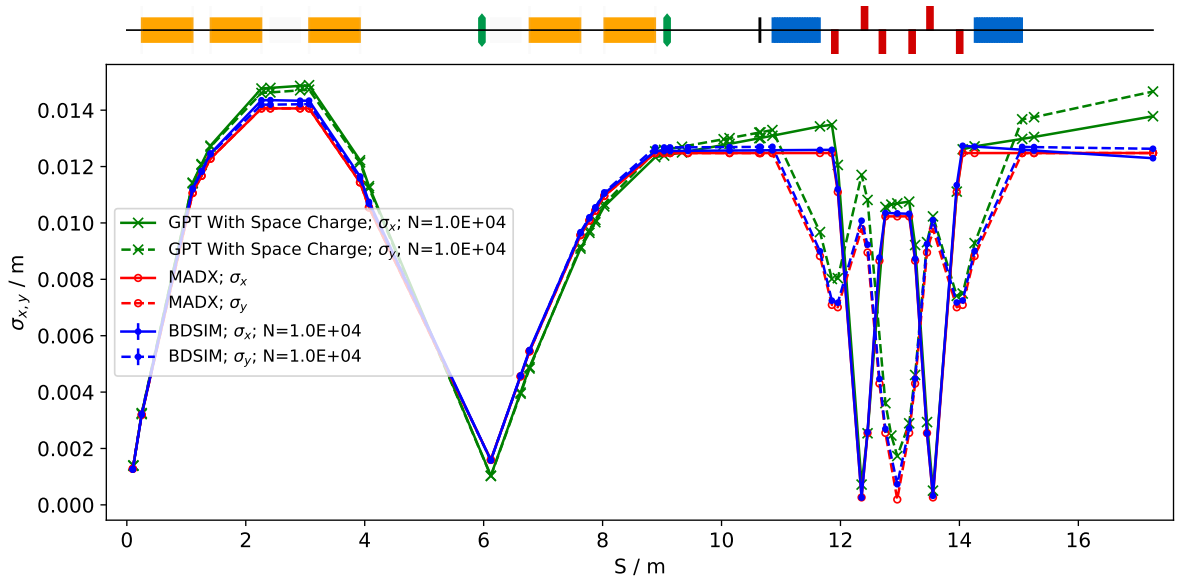

Figure 4. Horizontal (solid lines) and vertical (dashed lines) beam sizes through the *in vitro* beam transport, simulated including space-charge effects in GPT (green), and without space-charge in MADX (red) and BDSIM (blue).

The vertical arc uses transparent optics in an achromat matching section to ensure that the first-order transfer map through the arc is equivalent to the identity transformation and that any dispersive effects are cancelled. A 2 m drift tube is added after the arc to penetrate the concrete shielding of the end station floor and to bring the beam to bench height. The abort line consists of a drift space followed by a beam dump. Ramping down the first vertical dipole causes the beam to enter the dump and prevents particle transportation to the end station.

The underlying physics of plasma-lens operation cannot be simulated in BDSIM or GPT. It can, however, be approximated using solenoid magnets of equivalent strength. RF cavity fields were not simulated.

To produce the results shown here, 10 000 particles were simulated, corresponding to the estimated maximum bunch charge of 1×10^9 protons. Figure 4 shows excellent agreement between horizontal and vertical transverse beam sizes in BDSIM and MADX, verifying the beam line's performance in the absence of space-charge effects. Reasonable agreement between BDSIM and GPT is also seen when space-charge forces are included in GPT. Emittance growth is observed prior to the first solenoid, affecting the optical parameters throughout the machine. However, the resulting beam dimensions at the cell layer of 1.38 cm horizontally and 1.47 cm vertically are not significantly different from those in BDSIM. If needed, further adjustments of the Gabor lens and arc-quadrupole strengths may compensate for any space-charge effects. The transmission efficiency of the beam line is approximately 100%.

The small bunch dimensions in both transverse planes at the focus after the third Gabor lens, where the energy selection collimator will be placed, could be of concern if the effect of space-charge has been underestimated. Similar bunch dimensions are achieved in the vertical arc. Here, however, quadrupolar focusing is confined to a single plane to mitigate possible further emittance growth.

To investigate beam uniformity, BDSIM simulations with and without octupoles and collimation for beam shaping were conducted. Each octopole was assumed to have a magnetic length of 0.1 m and pole-tip radius of 5 cm. The strength parameter, k_3, of each octupole was arbitrarily set to 6000. A 2 cm thick iron

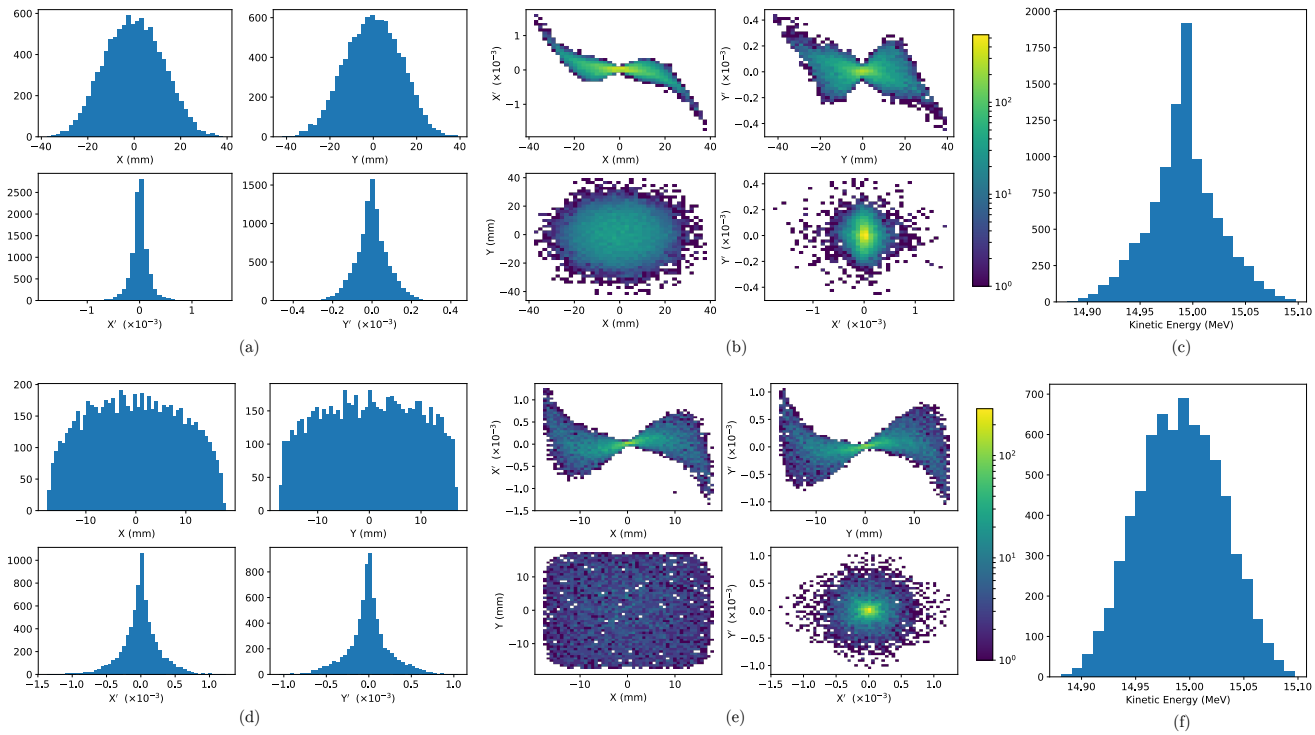

Figure 5. Beam phase space distributions at the end-station in the transverse plane, (X, Y); X′ and Y′ give the slope relative to the Z axis. The transverse phase space is shown in figures a and b for simulations without octupolar focusing and collimation, with the kinetic energy distribution shown in c. The same phase space distributions simulated with the effect of octupoles and collimation are in figures d, e, and f.

collimator with a 40 mm diameter aperture was positioned 1.5 m downstream of the octupole. Figure 5 shows the beam phase-space and particle distributions at the Stage 1 end station for the transverse and longitudinal axes with and without beam shaping. Without octupoles, the spatial profile is Gaussian, as expected. Inclusion of the octupoles and collimation system improves beam uniformity. The total beam width is 3.58 cm horizontally and 3.46 cm vertically, which is sufficient to irradiate one well in a six-well cell-culture plate. Further optimisation is required to improve uniformity whilst optimising beam-line transmission, which is approximately 70% for the results presented in figure 5.

An aberration can be seen in both transverse planes with and without beam shaping. This effect originates upstream of the octupoles in the solenoids used to approximate the Gabor lenses, and persists to the end station. The aberration is a concern, but is likely to change when the solenoids are replaced by full electromagnetic simulation of the Gabor lenses, at which point it will be further investigated.

The non-Gaussian energy distribution without beam shaping is a result of space-charge forces at the ion source; the distribution persists to the end station as no components which affect the longitudinal phase space were simulated. The Gaussian distribution seen with beam shaping reflects the effects of the collimation.

The proposed design is capable of delivering beams of the desired size to the *in vitro* end station. Space-charge effects affect the beam-transport performance but it is believed that these can be mitigated with minor adjustments to the Gabor lenses in the capture section. Initial studies indicate that a uniform beam can be delivered with further optimisation of the octupoles and collimator.

3.3.1 Alternative Design

To mitigate potential emittance growth from space-charge forces, an alternative beam line design was developed in which the final two Gabor lenses in the matching and energy selection section are replaced by four quadrupoles, limiting any bunch focusing to one plane at a time. The resulting machine is reduced in length to 15.4 m. Without space-charge effects, a beam width of 2.5 mm at the end station can be achieved. With space-charge, emittance growth prior to the first solenoid is once again observed leading to an increased beam size at the entrance of the first quadrupole, resulting in a spatially asymmetric and divergent beam at the end station. It is believed that the space-charge effects can be compensated by applying the same Gabor lens optimisation as in the baseline design and adjusting the quadrupole settings to deliver beam parameters similar to those achieved in the absence of space charge. The alternative design provides a solution that is more resilient to space-charge effects than the baseline, however, only the lower bound on the desired beam size has been achieved so far. For this design, further optimisation is required not only to improve optical performance but also to optimise octupole settings and to determine whether a beam with the desired uniformity can be delivered to the end station.

3.4 Post-acceleration and beam delivery to the *in vitro* and *in vivo* end stations

A fixed-field alternating-gradient accelerator (FFA), based on the spiral scaling principle [Krest et al. (1956); Symon et al. (1956); Fourrier et al. (2008); Tanigaki et al. (2006)], will be used to accelerate the beam in LhARA Stage 2 to obtain energies greater than the 15 MeV protons and 4 MeV/u carbon (C^{6+}) ions delivered by the laser-driven source. FFAs have many advantages for both medical and radiobiological applications such as: the capability to deliver high and variable dose; rapid cycling with repetition rates ranging from 10 Hz to 100 Hz or beyond; and the ability to deliver various beam energies without the use of energy degraders. An FFA is relatively compact due to the use of combined function magnets, which lowers the overall cost compared to conventional accelerators capable of delivering beams at a variety of energies such as synchrotrons. Extraction can be both simple and efficient and it is possible for multiple extraction ports to be provided. Furthermore, FFAs can accelerate multiple ion species, which is very important for radiobiological experiments and typically very difficult to achieve with cyclotrons.

A typical FFA is able to increase the beam momentum by a factor of three, though a greater factor may be achieved. For LhARA, this translates to a maximum proton-beam energy of 127 MeV from an injected beam of 15 MeV. For carbon ions (C^{6+}) with the same rigidity, a maximum energy of approximately 33.4 MeV/u can be produced.

The energy at injection into the FFA determines the beam energy at extraction. The injection energy will be changed by varying the focusing strengths in the Stage 1 beam line from the capture section through to the extraction line and the FFA ring. Appropriate adjustments to the frequency and phase of the RF in the FFA ring will also be made. This will allow the required energy slice from the broad spectrum produced at the laser-driven source to be captured and transported to the FFA. The FFA will then accelerate the beam, acting as a three-fold momentum multiplier. This scheme simplifies the injection and extraction systems since their geometry and location can be kept constant.

A second, 'high-energy', *in vitro* end station will be served by proton beams with a kinetic energy in the range 15–127 MeV and carbon-ion beams with energies up to 33.4 MeV/u. The extraction line from the FFA leads to a 90° vertical arc to send the beam to the high-energy *in vitro* end station. If the first dipole of the arc is not energised, the beam will be sent to the *in vivo* end station. The extraction line of the FFA includes a switching dipole that will send the beam to the high-energy-beam dump if it is not energised. The detailed design of the high-energy abort line, taking into account the requirement that stray radiation

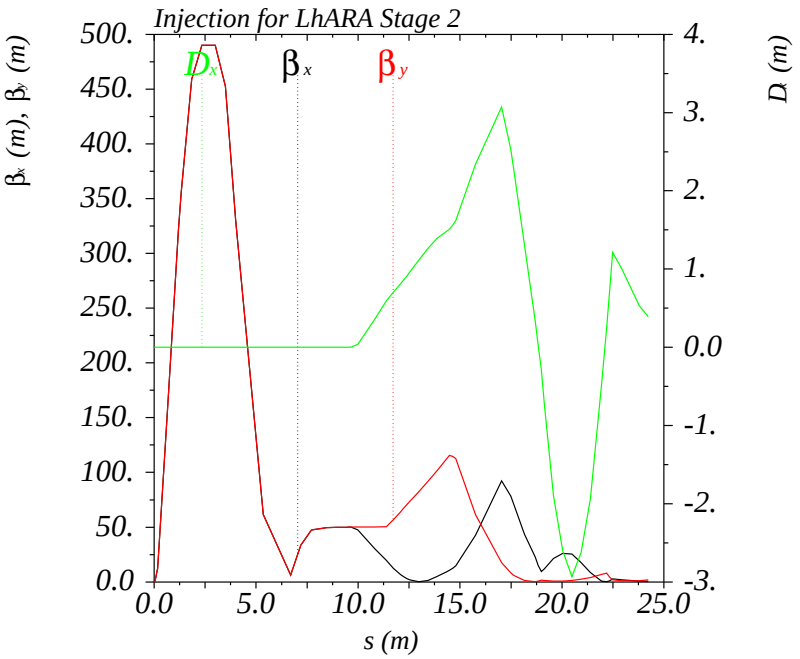

Figure 6. Twiss β_x and β_y functions and dispersion in the beam line consisting of the modified Stage 1 lattice and the transfer line allowing injection of the beam into the FFA ring. The distance s runs from the laser target to the exit of the injection septum.

does not enter the end stations, will be performed as part of the LhARA R&D programme.

3.4.1 Injection line

In order to inject the beam into the FFA, the settings of the Stage 1 beam line need to be adjusted to reduce the Twiss β function. The required Stage 1 optical parameters are shown in figure 6. The beam is diverted by a switching dipole into the injection line which transports the beam to the injection septum magnet. The injection line matches the Twiss β functions in both transverse planes and the dispersion of the beam to the values dictated by the periodic conditions in the FFA cell (figure 6). The presence of dispersion in the injection line allows a collimator to be installed for momentum selection before injection. The beam is injected from the inside of the ring, which requires that the injection line crosses one of the straight sections between the FFA magnets, see figure 7.

3.4.2 FFA ring

The magnetic field, B_y, in the median plane of a scaling spiral FFA is given by [Krest et al. (1956); Symon et al. (1956); Fourrier et al. (2008)]:

$$B_y = B_0 \left[\frac{R}{R_0}\right]^k F\left(\theta - \ln\left[\frac{R}{R_0}\right]\tan\zeta\right) \; ; \tag{3}$$

where B_0 is the magnetic field at radius R_0, k is the field index, ζ corresponds to the spiral angle and F is the 'flutter function'. This field law defines a zero-chromaticity condition, which means the working point

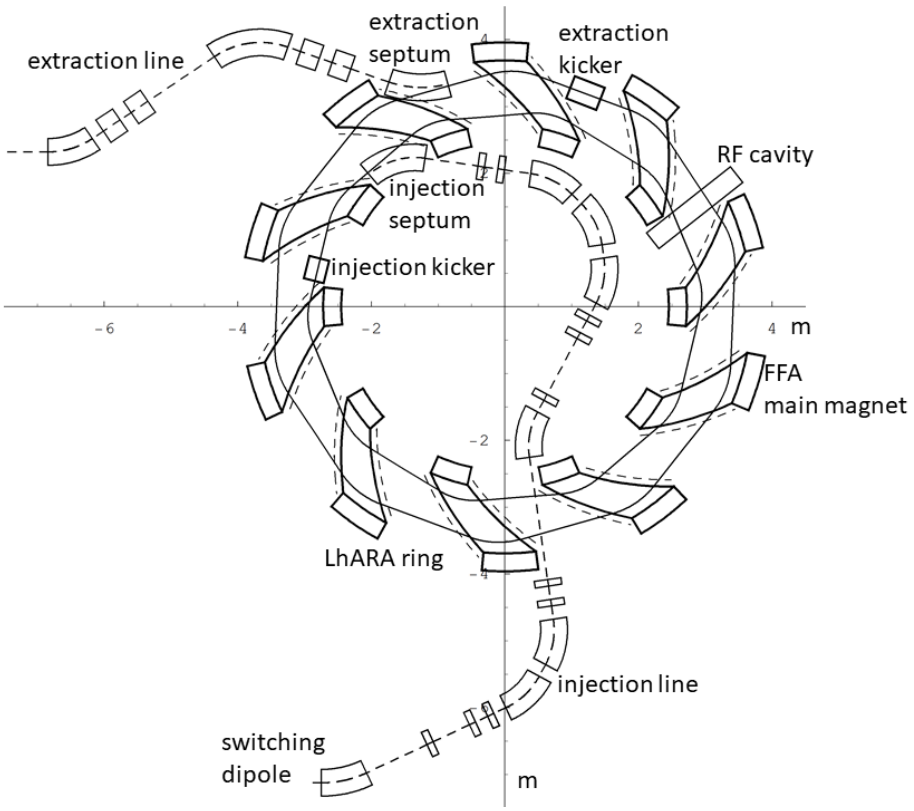

Figure 7. The layout of the injection line from the switching dipole to the injection septum together with the FFA ring, some of its subsystems and the first part of the extraction line.

of the machine is independent of energy (up to field errors and alignment imperfections). This avoids the need to cross any resonances, which would reduce the beam quality and could lead to beam loss.

Table 2 gives the main design parameters of the FFA ring. The ring consists of ten symmetric cells, each containing a single combined-function spiral magnet. The choice of the number of cells is a compromise between the size of the orbit excursion, which dictates the radial extent of the magnet, and the length of the straight sections required to accommodate the injection and extraction systems.

The betatron functions and dispersion in one lattice cell at injection are shown in figure 8(a). The tune diagram, showing the position of the working point of the machine in relation to the main resonance lines, is shown in figure 8(b). Tracking studies were performed using a step-wise tracking code in which the magnetic field is integrated using a Runge-Kutta algorithm [Lagrange et al. (2018)]. The magnetic field in the median plane was obtained using the ideal scaling law (equation 3). Enge functions were used to give the fringe fields. The field out of the median plane was obtained using Maxwell's equations and a 6^{th}-order Taylor expansion of the field. The dynamic acceptance for 100 turns, shown for the horizontal and vertical planes in figures 8(c) and 8(d), respectively, is significantly larger than the beam emittance. This statement holds even for the pessimistic scenario in which the emittance is assumed to be ten times larger than nominal. These results confirm that a good machine working point has been chosen.

A full aperture, fast injection of the beam will be performed using a magnetic septum, installed on the inside of the ring, followed by a kicker magnet situated in a consecutive lattice cell, as shown in figure 7. The specifications of the injection system are dictated by the parameters of the beam at injection, which are summarised for the nominal proton beam in table 3. The beam at injection has a relatively small emittance

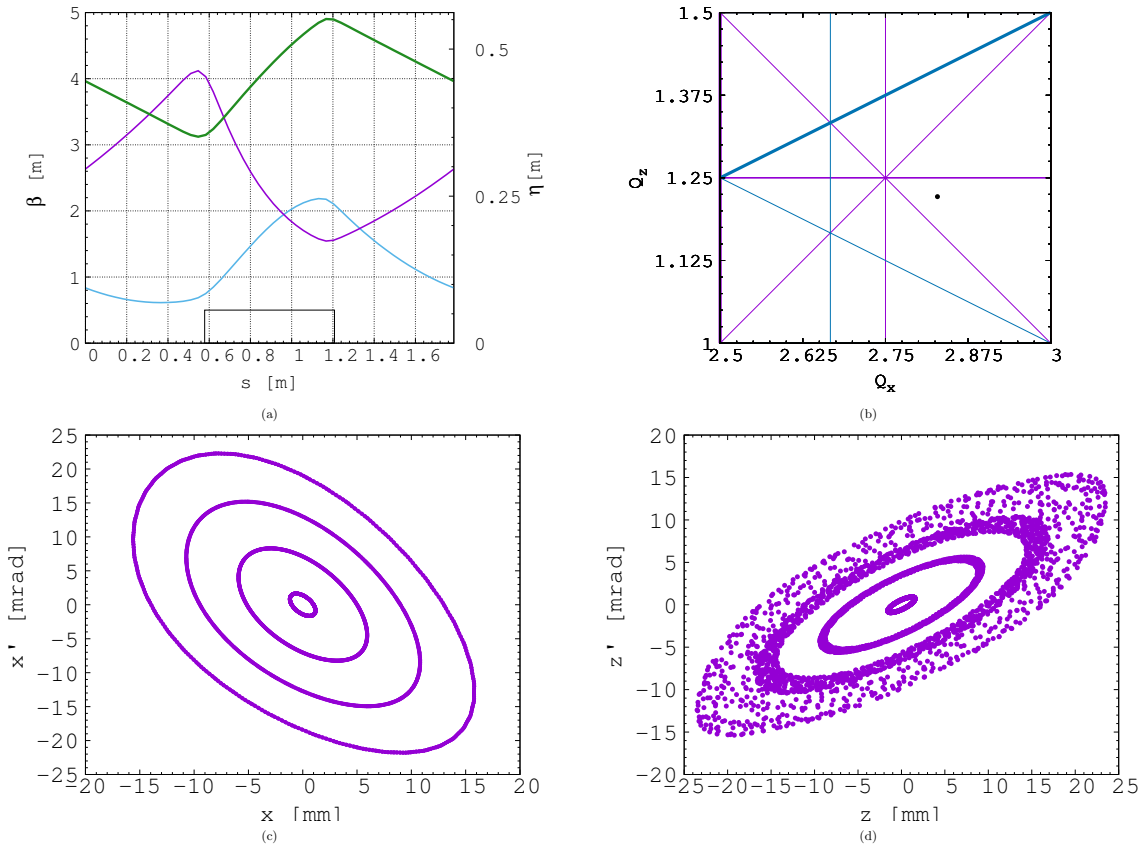

Figure 8. Beam optics and tracking in the FFA. Twiss β_h (blue), β_v (purple) functions and dispersion (green) in one lattice cell of the FFA ring (a). The working point of the FFA ring at (2.83, 1.22) on the tune diagram (b). The results of the horizontal (c) and vertical (d) dynamical acceptance study in the FFA ring, where a 1 mm offset is assumed in the vertical and horizontal planes respectively.

Table 3. Summary of the main parameters for the proton beam at the injection to the FFA ring. These parameters correspond to the nominal (maximum) acceleration mode of operation.

Parameter	Unit	Value
Beam energy	MeV	15
Total relative energy spread	%	± 2
Nominal physical RMS emittance (both planes)	π m rad	4.1×10^{-7}
Incoherent space charge tune shift		-0.8
Bunching factor		0.023
Total bunch length	ns	8.1
Bunch intensity		10^9

and short bunch length, which limits the intensity accepted by the ring due to the space-charge effect. An intensity of approximately 10^9 protons will be accepted by the ring assuming the nominal beam parameters. Space-charge effects will be severe immediately after injection, but will quickly be reduced due to the debunching of the beam. Fast extraction of the beam over the full aperture will be performed using a kicker magnet followed by a magnetic septum installed in a consecutive lattice cell close to the extraction orbit.

Acceleration of the beam to 127 MeV will be done using an RF system operating at harmonic number $h = 1$ with an RF frequency range from 2.89 MHz to 6.48 MHz. The RF voltage required for 10 Hz

Table 4. Beam emittance values and target β values for different beam sizes for 40 MeV and 127 MeV beams. The beam size is taken to be four times the sigma of the transverse beam distribution.

	40 MeV protons (Nominal)	127 MeV protons (Nominal)	127 MeV protons (Pessimistic)
RMS Emittance (ϵ_x, ϵ_y) [π mm mrad]	0.137	0.137	1.37
β [m] for a 1 mm spot size	0.46	0.46	0.039
β [m] for a 10 mm spot size	46	46	4.5
β [m] for a 30 mm spot size	410	410	40

operation is 0.5 kV. However, at this relatively low voltage the energy acceptance at injection is $\pm 0.7\%$. Operating with a voltage of 4 kV increases the energy acceptance to $\pm 2\%$. This voltage can be achieved with one cavity [Yonemura et al. (2008)]. Here, two cavities are proposed to provide greater operational stability. Normal conducting spiral-scaling FFA magnets, similar to the ones needed for LhARA, have been successfully constructed [Tanigaki et al. (2006); Planche et al. (2009)] using either distributed, individually-powered coils on a flat pole piece or using a conventional gap-shaping technique. For the LhARA FFA, we propose a variation of the coil-dominated design recently proposed at the Rutherford Appleton Laboratory in R&D studies for the upgrade of the ISIS neutron and muon source. In this case, the nominal scaling field is achieved using a distribution of single-powered windings on a flat pole piece. The parameter k can then be tuned using up to three additional independently-powered windings. The extent of the fringe field across the radius of the magnet must be carefully controlled using a 'field clamp' to achieve zero chromaticity. An active clamp, in which additional windings are placed around one end of the magnet, may be used to control the flutter function and thereby vary independently the vertical tune of the FFA ring. The FFA is required to deliver beams over a range of energy; each energy requiring a particular setting for the ring magnets. Therefore, a laminated magnet design may be required to reduce the time needed to change the field. The magnet gap of 4.7 cm given in table 2 is estimated assuming a flat-pole design for the magnet.

3.4.3 Extraction Line

Substantial margins in the beam parameters were assumed in the design of the extraction line from the FFA due to uncertainties in the beam distributions originating from the Stage 1 beam transport, the FFA injection line, and potential distortions introduced by the presence of space-charge effects during acceleration in the ring. The beam emittance was therefore allowed to be as large as a factor of ten greater than the nominal value, which was derived by assuming that the normalised emittance is conserved from the source, through the Stage 1 beam line, and in the FFA ring. In the nominal case, the physical emittance of the beam is affected by adiabatic damping only. Substantial flexibility in the optics of the extraction line is required, as the extraction line must accommodate a wide spectrum of beam conditions to serve the *in vitro* and *in vivo* end-stations.

Detailed studies were carried out for proton beams with kinetic energies of 40 MeV and 127 MeV. Table 4 gives the Twiss β values for different beam sizes for the 40 MeV and 127 MeV proton-beam energies assuming a Gaussian beam distribution. The optics and geometric acceptance of the system is approximately the same for the 40 MeV and 127 MeV beams, justifying the working hypothesis that beam emittance is approximately the same for both beam energies. This assumption will be revised as soon as space-charge simulations for the entire system are available.

The first two dipoles and four quadrupoles of the extraction line bend the beam coming from the extraction septum of the FFA such that it is parallel to the low-energy beam line while ensuring that dispersion is

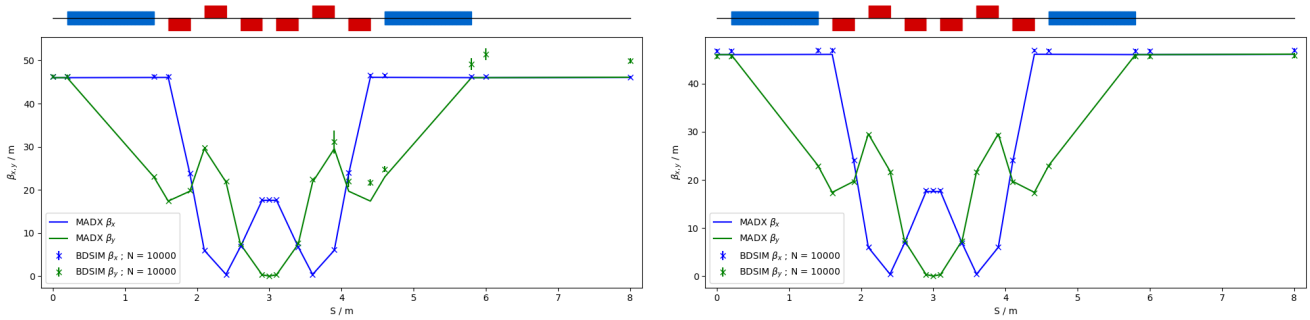

Figure 9. Comparison of MADX and BDSIM simulation of 40 MeV (left) and a nominal 127 MeV (right) proton beam passing through the high energy *in vitro* arc simulated with 10^4 particles (in BDSIM).

closed. Closing the dispersion is critical, as off-momentum particles will follow trajectories different to those followed by particles with the design momentum and therefore impact the size and shape of the beam downstream. The second part of the extraction line consists of four quadrupoles which transport the beam either to the first dipole of the vertical arc that serves the high-energy *in vitro* end station or to the *in vivo* end station if this dipole is not energised. These quadrupoles provide the flexibility required to produce the different beam sizes for the *in vitro* end station, as specified in table 4.

3.4.4 High-energy *in vitro* beam line

The high-energy *in vitro* beam line transports the beam from the extraction line to the high-energy *in vitro* end station. The 90° vertical bend is a scaled version of the low-energy vertical arc, following the same design principles, and also consists of two bending dipole magnets and six quadrupole magnets. To accommodate the higher beam energies, the lengths of the magnets were scaled in order to ensure that peak magnetic fields were below the saturation limits of normal conducting magnets. The bending dipole magnet lengths were increased to 1.2 m each and the quadrupole lengths were tripled to 0.3 m. The overall length of the arc then becomes 6 m, compared to 4.6 m for the low energy *in vitro* arc. This difference in arc length means the high-energy *in vitro* arc finishes about 0.9 m higher than the low-energy one. This difference can easily be accommodated by adjusting the final drift lengths.

The quadrupole strengths for the scaled high-energy *in vitro* arc were obtained using MADX calculations, tracking simulations using BDSIM show good agreement with these, see figure 9. The input beam distribution used in BDSIM was assumed to be Gaussian with Twiss $\beta = 46$, which gives a beam size of about 10 mm. Small deviations from the BDSIM results were observed in GPT simulations due to space-charge effects.

3.4.5 *In vivo* beam line

To facilitate efficient small-animal handling, the end station dedicated to *in vivo* experiments will be positioned adjacent to the principle road access to the facility. If the first dipole of the high-energy *in vitro* arc is not energised, the beam is sent to the *in vivo* end station. From the end of the extraction line, 7.7 m of drift is necessary to clear the first bending dipole of the *in vitro* arc, to provide space for the five RF cavities needed for longitudinal phase-space manipulation and to allow space for diagnostic devices. Following this drift is a further 6.6 m of beam line that includes four quadrupoles, each of length 0.4 m, which are used to perform the final focusing adjustments of the beam delivered to the *in vivo* end station. A final 1.5 m drift length is reserved for scanning magnets so spot scanning can be performed and to allow for penetration of the shielding of the *in vivo* end station. In total, the *in vivo* beam line is 15.6 m in length.

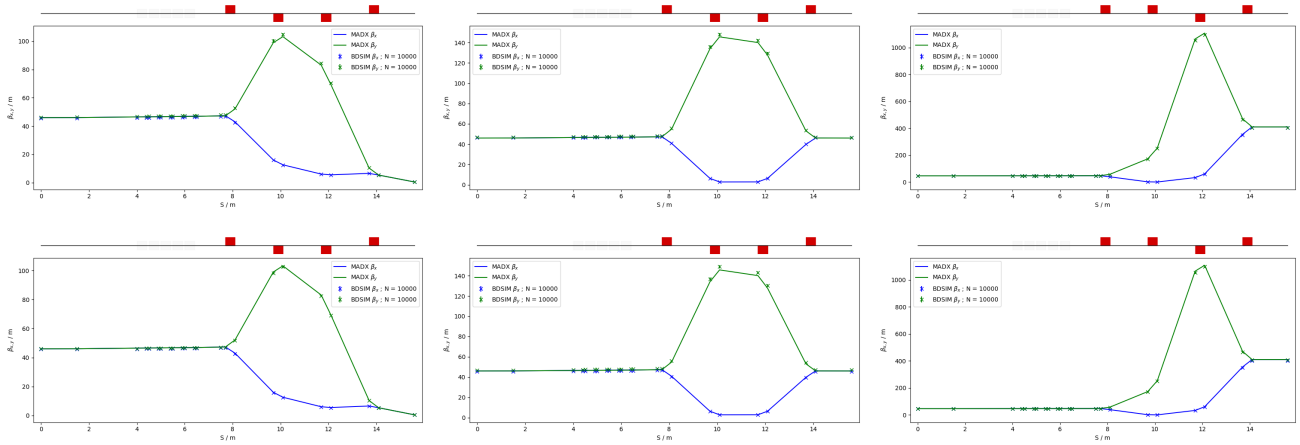

Figure 10. MADX and BDSIM simulations of the *in vivo* beam line for a 40 MeV proton beam (top row) and a nominal 127 MeV proton beam (bottom row) with quadrupoles matched to obtain $\beta_{x,y} = 0.46$ m (left), $\beta_{x,y} = 46$ m (middle) and $\beta_{x,y} = 410$ m (right) at the end of the beam line for 10^4 particles.

The flexible design can match the various $\beta_{x,y}$ values given in table 4, but not the smallest target value of $\beta_{x,y} = 0.039$ m for the pessimistic scenario, which is very challenging. To verify that the optics design can provide the required beam sizes, simulations were performed with BDSIM using an input Gaussian beam generated with the Twiss β values given in tables 4. Figure 10 shows the results for a 40 MeV proton beam and a nominal emittance 127 MeV proton beam matched in order to obtain beam sizes of 1 mm, 10 mm and 30 mm.

3.5 Instrumentation

Commercial off-the-shelf (COTS) instrumentation will be used for Stages 1 and 2 of LhARA wherever possible. However, the characteristics of the beam (e.g. very high charge-per-bunch, low-to-moderate energy) will require that some custom solutions be developed. The authors are developing two concepts, termed SciWire and SmartPhantom, for the low- and high-energy *in vitro* end stations, respectively. These detectors can also be used for beam diagnostics and may find application at other facilities. Instrumentation for the detection of secondary particles arising from the interaction of the beam with tissue is not discussed here but is an important area that will be studied in the future.

3.5.1 SciWire

For the Stage 1 beam, the maximum proton energy is 15 MeV. Shot-to-shot characterisation of the beam is essential and requires the use of a very thin detector with a fast response. The SciWire [Kurup (2019)] is being developed to provide energy and intensity profile measurements for low-energy ion beams. A single SciWire plane consists of two layers of 250 μm square-section scintillating fibres, with the fibre directions in the two layers orthogonal to each other. A series of back-to-back planes provides a homogeneous volume of scintillator. If there are enough planes to stop the beam, the depth of penetration will allow the beam energy to be inferred. This is a destructive measurement so would only be performed when experiments are not running. A single plane, however, can be used for 2D beam-profile measurements while the beam is being delivered for experiments. Light from the SciWire fibres may be detected using a CMOS camera or photodiodes. If the instrumentation is sufficiently fast, the SciWire can be used to derive feedback signals for beam tuning.

3.5.2 SmartPhantom

To study the dose profile of Stage 2 beams in real time, the SmartPhantom [Barber et al. (2018)] is being developed. This is a water-filled phantom, instrumented with planes of scintillating fibres, used to infer the dose distribution with distance. The detection elements of the SmartPhantom are 250 μm diameter, round scintillating fibres. Each fibre station consists of two planes of fibres, in which the fibre directions are orthogonal. Five fibre stations are arranged in the phantom in front of the cell-culture flask. The fibres may be coupled to photodiodes, or a CMOS camera. Simulations in GEANT4 are being used to develop analysis techniques to determine the position of the Bragg peak shot-by-shot. The beam profile and dose delivered can then be calculated in real time.

3.5.3 Beam line Instrumentation

The requirement for instrumentation begins with the Ti:Sapphire laser. The laser focal spot will be characterised using a camera-based system and high-speed wavefront measurements [Wang (2014)] from COTS vendors.

For the Stage 1 beam line, beam position monitors (BPMs) will be needed for beam steering. Because of the low beam energy, non-intercepting BPMs using capacitive pickup buttons will be used. Custom pickups will be needed to match the beam pipe geometry, but COTS electronics are available. The beam current will be monitored near the end of each beam line, using integrating current toroids (ICT), backed up with the option of insertable multi-layer Faraday cups (MLFC) to give absolute beam current and energy measurements. Beam profiles could be measured by secondary emission monitor (SEM) grids on both Stage 1 and Stage 2 beam lines. For Stage 1, these monitors will be mounted on pneumatic actuators to avoid scattering. Each end station could be equipped with insertable "pepper-pot" emittance monitors and a transverse deflection cavity with fluorescent screen could be provided for bunch shape measurements.

The BPMs on the FFA will require pickup designs suitable for the unusual, wide and shallow vacuum vessel. The FFA at the KURNS facility in Kyoto has a similar layout [Uesugi (2018)] and uses a kicker and capacitive pickup to perform tune measurements in each transverse direction. A minimum of one BPM every second cell will be used in the FFA so that the beam orbit can be measured. BPMs will also be required close to the injection and extraction septa. The BPM system may be able to use COTS electronics, but the pickups will be based on the KURNS design of multiple electrodes arranged across the vacuum vessel width.

The data acquisition system needs to be able to store calibration data and apply corrections in real time. It is necessary to be able to find the beam centre from a profile, even when the profile may be non-Gaussian and possibly asymmetric. Field programmable gate arrays (FPGAs) can be used to perform fast fitting and pattern recognition of beam profiles. The instrumentation will be integrated with the accelerator control system and will provide fast feedback and adjustment of the beam parameters in real time.

3.6 Biological end stations

In order to deliver a successful radiobiological research programme, high-end and fully equipped *in vitro* and *in vivo* end-stations will be housed within the LhARA facility. The two *in vitro* end-stations (high and low energy) will contain vertically-delivered beam lines which will be used for the irradiation of 2D monolayer and 3D-cell systems (spheroids and patient-derived organoids) in culture. The beam line within the end-stations will be housed in sealed units that will be directly sourced with appropriate gases (carbon dioxide and nitrogen), allowing the cells within culture plates to be incubated for a short time in stable conditions prior to and during irradiation. This will also enable the chamber to act, where necessary, as a

hypoxia unit (e.g. 0.1%–5% oxygen concentration). Furthermore, these sealed units will contain robotics to enable the numerous cell culture plates housed within to be placed into and taken out of the beam.

The *in vitro* end-stations will be located within a research laboratory equipped with state-of-the-art facilities. The laboratory will include all the necessary equipment for bench-top science, sample processing and analysis (e.g. refrigerated centrifuges and light/fluorescent microscopes), along with the equipment required for contaminant-free cell culture (e.g. humidified CO_2 cell culture incubators, Class II biological safety cabinets), and for the storage of biological samples and specimens (e.g. $-20°$C and $-80°$C freezers and fridges). The laboratory will also house an X-ray irradiator (allowing direct RBE comparisons between conventional photon irradiation, and the proton and carbon ions delivered by the accelerator), a hypoxia chamber (for long-term hypoxia studies), a robotic workstation (for handling and processing of large sample numbers, aiding high-throughput screening experiments), and an ultra-pure-water delivery system. These facilities will enable a myriad of biological end-points to be investigated in both normal- and tumour-cell models not only from routine clonogenic survival and growth assays, but also from significantly more complex end-points (e.g. inflammation, angiogenesis, senescence and autophagy).

The *in vivo* end-station will be served with relatively high-energy proton and carbon ions capable of penetrating deeper into tissues allowing the irradiation of whole animals. The ability to perform *in vivo* pre-clinical studies is vital for the future effective translation of the research into human cancer patients where optimum treatment strategies and the reduction of side-effects are crucial. The *in vivo* end-station will allow the irradiation of a number of small-animal models (e.g. xenograft mouse and rat models) which can further promote an examination of particular ions on the appropriate biological end-points (e.g. tumour growth and normal tissue responses). The end-station will contain a small-animal handling area which will allow for the anaesthetisation of animals prior to irradiation. To enable the irradiation of small target volumes with a high level of precision and accuracy, an image guidance system (e.g. computed tomography) will be available. The animals will subsequently be placed in temperature-controlled holder tubes enabling the correct positioning of the relevant irradiation area in front of the beam line. The beam size is sufficient to give flexibility in the different irradiation conditions, in particular through passive scattering, pencil-beam scanning, and micro-beam irradiation, to be investigated at both conventional and FLASH dose rates. It is envisaged that the animals will be taken off-site post-irradiation to a nearby animal-holding facility for a follow-up period where biological measurements will be conducted.

3.7 Infrastructure and integration

The LhARA facility will encompass two floors of roughly 42 m in length and 18 m in width. The ground floor will contain the laser, accelerator, and *in vivo* end station while the first floor will house the laboratory area and the two *in vitro* end stations. The entire facility will require radiation protection in the form of concrete shielding. There will be three principal areas: a radiation controlled-access area, a laser controlled-access area, and a laboratory limited-access area.

For a facility such as LhARA laser, radiation and biological safety are primary concerns. It is envisaged that LhARA will be built at a national laboratory or equivalent research institute which has an established safety-management system and culture in place.

The infrastructure and integration of the LhARA facility will require R&D in four key areas: risk analysis (project risks), risk assessments (safety risks), radiation simulations, and controls development. The risk analysis will cover all aspects of the facility, such as funding and resource availability, not just technical risks. A safety-risk assessment will be performed to describe and control all potential safety risks in the

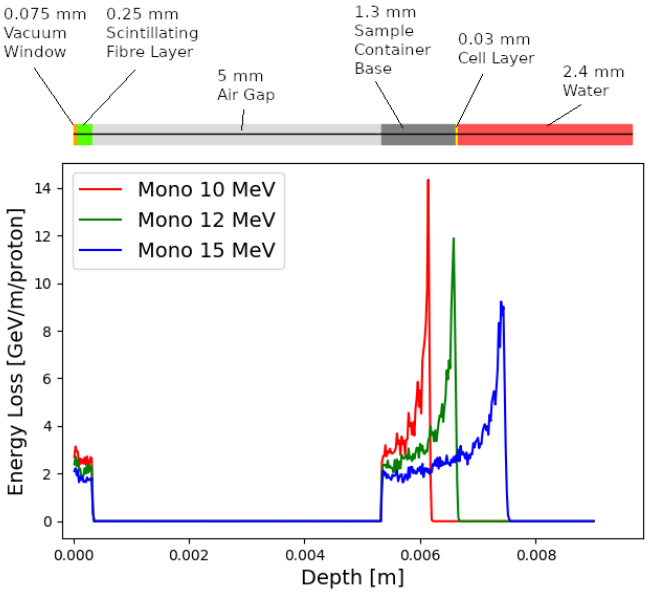

Figure 11. Energy loss as a function of depth in the low-energy *in vitro* end station for three mono-energetic proton energies: 10 MeV; 12 MeV; and 15 MeV. Each beam was simulated using 10^4 particles at the start of the end station. The material through which the beam passes is indicated above the figure. The vacuum window is plotted at a depth value of 0 m. The beam deposits energy in the vacuum window and the layer of scintillating fibre before passing through an air gap and entering the sample container.

facility. The safety-risk assessment will, to a reasonable degree, identify all pieces of equipment that require safety mitigations and identify control measures that must be put in place. Coupled closely with the safety-risk assessment, radiation simulations will be developed to characterise the radiation hazards in and around the LhARA facility. The last area to require R&D will be the control systems. It is expected that the facility will use the Experimental Physics and Industrial Control System [The EPICS collaboration (2020)], which can be further developed at this stage.

4 PERFORMANCE

The dose distributions delivered to the end stations were evaluated using BDSIM. Figure 11 shows the energy lost by the beam as it enters the low-energy *in vitro* end station. The beam passes through the vacuum window, a layer of scintillating fibre, and a 5 mm air gap. The beam then enters the cell-sample container, assumed to be polystyrene, which supports a 30 μm thick layer of cells, modelled using the GEANT4 material "G4_SKIN_ICRP" [NIST (2017)]. The transverse momentum of protons in the beam was assumed to follow a Gaussian distribution, with a lateral spread small enough for the beam to be fully contained within the required spot size of 3 cm. Figure 11 shows that a proton beam with 10 MeV kinetic energy does not reach the cell layer. The Bragg peak of a 12 MeV proton beam is located close to the cell layer, while a 15 MeV beam, the maximum energy specified for delivery to the low-energy *in vitro* end station, has a Bragg peak located beyond the cell layer. LhARA's ability to deliver various beam energies will allow the investigation of the radiobiological effects of irradiation using different parts of the Bragg peak, effectively varying the LET across the sample. RF cavities are placed in both the stage 1 and the stage 2 beam lines to allow the manipulation of the energy of the bunch as a function of time. This facility will allow the study of the impact of a "spread-out Bragg peak" (SOBP).

The maximum dose that can be delivered was evaluated for a variety of beam energies. In order for the dose to be reported in units of Gray it is necessary to define the volume within which the energy deposition is to be integrated. Therefore, the dose was estimated from simulations by calculating the energy deposited in a volume of water corresponding in size to the sensitive volume of a PTW 23343 Markus ion chamber [GmbH (2019/2020)] placed at the position of the Bragg peak in each case. This choice allows the doses and dose-rates reported here to be compared to those of operating facilities. The cylindrical sensitive volume of the ion chamber has a radius of 2.65 mm and a depth of 2 mm, giving a volume of about 4.4×10^{-8} m^3. The total energy deposited within the chamber was recorded and converted into dose in units of Gray.

For the low-energy *in vitro* end station, the minimum spot size has a diameter of 10 mm, which is larger than the area of the chamber. A single shot of 10^9 protons at 12 MeV with this spot size deposits 3.1×10^{-4} J in the chamber volume, corresponding to a dose of 7.1 Gy. For this simulation, the thickness of the sample container was reduced so that the Bragg peak could be positioned within the chamber volume. For the bunch length of 7.0 ns, the maximum instantaneous dose rate is 1.0×10^9 Gy/s and the average dose rate is 71 Gy/s, assuming a repetition rate of 10 Hz. A single shot of 10^9 protons at 15 MeV deposits 5.6×10^{-4} J in the chamber volume, corresponding to a dose of 12.8 Gy. This gives an instantaneous dose rate of 1.8×10^9 Gy/s and an average dose rate of 128 Gy/s assuming the same bunch length and repetition rate as for the 12 MeV case.

For the high-energy *in vitro* end station, a similar design to the low-energy end station was used, but the air gap was increased from 5 mm to 5 cm and a water phantom was placed at the end of the air gap instead of a cell culture plate. The water phantom used in the simulation was based upon the PTC T41023 water phantom [PTW (2009)]. In addition, the smaller minimum design beam size of 1 mm was used. A single shot of 10^9 protons at 127 MeV deposits 6.9×10^{-4} J in the chamber at the pristine Bragg peak depth, corresponding to a dose of 15.6 Gy, an instantaneous dose rate of 3.8×10^8 Gy/s and an average dose rate of 156 Gy/s. The end-station design assumed for a 33.4 MeV/u carbon beam was the same as that used for the low-energy *in vitro* end station due to the limited range in water of the carbon beam. The intensity of the beam is assumed to be a factor of 12 less than that for protons in order to preserve the same strength of the space-charge effect at injection into the FFA with the same beam parameters because the incoherent space charge tune shift is proportional to q^2/A and inversely proportional to $\beta^2\gamma^3$, where q is the particle charge, A its mass number, and β and γ its relativistic parameters. A single pulse of 8.3×10^7 ions deposits 3.2×10^{-3} J at the depth of the pristine Bragg peak, leading to an instantaneous dose rate of 9.7×10^8 Gy/s and a maximum average dose rate of 730 Gy/s.

The expected maximum dose rates are summarised in table 5. The instantaneous dose rates depend on the bunch length which differs depending on the energies. For the low-energy *in vitro* line, a 7 ns bunch length is assumed for all energies. For the higher energies, a 127 MeV proton beam is delivered with a bunch length of 41.5 ns, and a bunch length of 75.2 ns for a 33.4 MeV/u carbon beam. The same repetition rate of 10 Hz was used for all energies. The minimum beam size at the start of the end station for the 12 MeV and 15 MeV proton-beam simulations was 1 cm. A 1 mm beam size was used for the 127 MeV proton beam and 33.4 MeV/u carbon-ion beam simulations.

5 CONCLUSIONS

The initial conceptual design of LhARA, the Laser-hybrid Accelerator for Radiobiological Applications, has been described and its performance evaluated in simulations that take into account the key features

Table 5. Summary of expected maximum dose per pulse and dose rates that LhARA can deliver for minimum beam sizes. These estimates are based on Monte Carlo simulations using a bunch length of 7 ns for 12 MeV and 15 MeV proton beams, 41.5 ns for the 127 MeV proton beam and 75.2 ns for the 33.4 MeV/u carbon beam. The average dose rate is based on the 10 Hz repetition rate of the laser source.

	12 MeV Protons	15 MeV Protons	127 MeV Protons	33.4 MeV/u Carbon
Dose per pulse	7.1 Gy	12.8 Gy	15.6 Gy	73.0 Gy
Instantaneous dose rate	1.0×10^9 Gy/s	1.8×10^9 Gy/s	3.8×10^8 Gy/s	9.7×10^8 Gy/s
Average dose rate	71 Gy/s	128 Gy/s	156 Gy/s	730 Gy/s

of the facility. LhARA uses a laser-driven source to create a large flux of protons or light ions which are captured and formed into a beam by strong-focusing plasma lenses, thus evading prevalent space-charge limits on the instantaneous dose rate that can be delivered. Acceleration, performed using a fixed-field alternating-gradient accelerator, preserves the unique flexibility in the time, spectral, and spatial structure of the beam afforded by the laser-driven source. The ability to trigger the laser pulse that initiates the production of protons or ions at LhARA will allow the time structure of the beam to be varied to interrupt the chemical and biological pathways that determine the biological response to ionising radiation. The almost parallel beam that LhARA will deliver can be varied to illuminate a circular area with a maximum diameter of between 1 cm and 3 cm with an almost uniform dose, or focused to a spot with diameter of $\sim$ 1 mm. These features will allow radiobiological studies to be carried out in completely new regimens, delivering a variety of ion species in a broad range of time structures and spatial configurations at instantaneous dose rates up to and potentially significantly beyond the current ultra-high dose-rate "FLASH" regime.

The enhanced understanding these studies will provide, may in turn result in new approaches to radiotherapy, decreasing the radio-toxicity for normal tissue while maintaining or enhancing the tumour-control probability. Further, by developing a triggerable system that incorporates dose-deposition imaging in a fast feedback-and-control system, in the long term LhARA has the potential to remove the requirement for a large gantry for proton and ion therapy, laying the foundations for "best in class" treatments to be made available to the many by reducing the footprint of future particle-beam therapy systems.

The radiobiology programme in combination with the demonstration in operation of the laser-hybrid technique means that the LhARA programme has the potential to drive a step-change in the clinical practice of proton- and ion-beam therapy.

ACKNOWLEDGEMENTS

The work described here was made possible by a grant from the Science and Technology Facilities Council (ST/T002638/1,ST/P002021/1). Additional support was provided by the STFC Rutherford Appleton and Daresbury Laboratories and members of the LhARA consortium. We gratefully acknowledge all sources of support. A pre-publication review of the pre-CDR for LhARA was carried out by P. Bolton (LMU, Munich), M. Lamont (CERN), Y. Prezado (Institut Curie), and F. Romano (INFN-LNS and the National Physical Laboratory). We are grateful to the review panel for their support and detailed feedback on the draft pre-CDR.

REFERENCES

[Dataset] A-SAIL Project (2020). A-sail project. https://www.qub.ac.uk/research-centres/A-SAILProject/

Amin, T., Barlow, R., Ghithan, S., Royb, G., and Schuhb, S. (2018). Formation of a uniform ion beam using octupole magnets for bioleir facility at cern. *JINST* 13, P04016

Atun, R., Jaffray, D. A., Barton, M. B., Bray, F., Baumann, M., Vikram, B., et al. (2015). Expanding global access to radiotherapy. *The Lancet Oncology* 16, 1153 – 1186. doi:https://doi.org/10.1016/S1470-2045(15)00222-3

Autin, B., Carli, C., D'Amico, T., Gröbner, O., Martini, M., and Wildner, E. (1998). *BeamOptics: A program for analytical beam optics*. Tech. Rep. CERN–98-06, European Organization for Nuclear Research (CERN). http://inis.iaea.org/search/search.aspx?orig_q=RN:30052986

Barber, G. et al. (2018). *Outline design and cost estimate for the SmartPhantom*. Tech. Rep. CCAP-TN-INST-01, The Centre for the Clinical Application of Particles, Imperial College London, London, UK. Available online at: https://ccap.hep.ph.ic.ac.uk/trac/raw-attachment/wiki/Communication/Notes/SmartPhantom.pdf

Berry, R. J. (1973). EFFECTS OF RADIATION DOSE-RATE: From Protracted, Continuous Irradiation to Ultra-High Dose-Rates from Pulsed Accelerators. *British Medical Bulletin* 29, 44–47. doi:10.1093/oxfordjournals.bmb.a070955

Bin, J., Allinger, K., Assmann, W., Dollinger, G., Drexler, G. A., Friedl, A. A., et al. (2012). A laser-driven nanosecond proton source for radiobiological studies. *Applied Physics Letters* 101, 243701. doi:10.1063/1.4769372

Bin, J., Ma, W., Wang, H., Streeter, M., Kreuzer, C., Kiefer, D., et al. (2015). Ion Acceleration Using Relativistic Pulse Shaping in Near-Critical-Density Plasmas. *Physical Review Letters* 115, 064801. doi:10.1103/PhysRevLett.115.064801

Bourhis, J., WJ, S., PG, J., O, G., C, B., F, D., et al. (2019). Treatment of a first patient with FLASH-radiotherapy. *Radiotherapy and oncology : journal of the European Society for Therapeutic Radiology and Oncology* 139. doi:10.1016/J.RADONC.2019.06.019

Bray, F., Ferlay, J., Soerjomataram, I., Siegel, R. L., Torre, L. A., and Jemal, A. (2018). Global cancer statistics 2018: GLOBOCAN estimates of incidence and mortality worldwide for 36 cancers in 185 countries. *CA: A Cancer Journal for Clinicians* 68, 394–424. doi:10.3322/caac.21492

Bulanov, S., Esirkepov, T., Khoroshkov, V., Kuznetsov, A., and Pegoraro, F. (2002). Oncological hadrontherapy with laser ion accelerators. *Physics Letters A* 299, 240–247. doi:https://doi.org/10.1016/S0375-9601(02)00521-2

Carter, R. J., Nickson, C. M., Thompson, J. M., Kacperek, A., Hill, M. A., and Parsons, J. L. (2018). Complex dna damage induced by high linear energy transfer alpha-particles and protons triggers a specific cellular dna damage response. *International Journal of Radiation Oncology*Biology*Physics* 100, 776 – 784. doi:https://doi.org/10.1016/j.ijrobp.2017.11.012

Chaudhary, P., Gwynne, D., Doria, D., Romagnani, L., Maiorino, C., Padda, H., et al. (2017). Effectiveness of laser accelerated ultra high dose rate protons in DNA DSB damage induction under hypoxic conditions. In *44th EPS Conference on Plasma Physics, EPS 2017* (Belfast, United Kingdom: European Physical Society (EPS)), vol. 44F. P1.217

Chaudhary, P., Marshall, T. I., Perozziello, F. M., Manti, L., Currell, F. J., Hanton, F., et al. (2014). Relative Biological Effectiveness Variation Along Monoenergetic and Modulated Bragg Peaks of a 62-MeV Therapeutic Proton Beam: A Preclinical Assessment. *International Journal of Radiation Oncology • Biology • Physics* 90, 27–35. doi:10.1016/j.ijrobp.2014.05.010

Chen, S. N., Vranic, M., Gangolf, T., Boella, E., Antici, P., Bailly-Grandvaux, M., et al. (2017). Collimated protons accelerated from an overdense gas jet irradiated by a 1 μm wavelength high-intensity short-pulse laser. *Scientific Reports* 7, 13505. doi:10.1038/s41598-017-12910-6

Cirrone, G., Catalano, R., Cuttone, G., Margarone, D., Schillaci, F., and Petringa, G. (2020). Generation control and application of flash radiation beam from laser-matter interaction: The ELIMAIA-ELIMED beamline. *Nuovo Cim. C* 43, 15. doi:10.1393/ncc/i2020-20015-6

Cirrone, G. et al. (2016). Status, Plans and Potential Applications of the ELIMED Beam Line at ELI-Beamlines. In *7th International Particle Accelerator Conference* (Busan, Korea), WEXB01. doi:10.18429/JACoW-IPAC2016-WEXB01

Cirrone, G. A. P., Margarone, D., Maggiore, M., Anzalone, A., Borghesi, M., Jia, S. B., et al. (2013). ELIMED: a new hadron therapy concept based on laser driven ion beams. In *Laser Acceleration of Electrons, Protons, and Ions II; and Medical Applications of Laser-Generated Beams of Particles II; and Harnessing Relativistic Plasma Waves III*, eds. E. Esarey, C. B. Schroeder, W. P. Leemans, K. W. D. Ledingham, and D. A. Jaroszynski. International Society for Optics and Photonics (Prague, Czech Republic: SPIE), vol. 8779, 216 – 225. doi:10.1117/12.2026530

Clark, E. L., Krushelnick, K., Davies, J. R., Zepf, M., Tatarakis, M., Beg, F. N., et al. (2000a). Measurements of energetic proton transport through magnetized plasma from intense laser interactions with solids. *Phys. Rev. Lett.* 84, 670–673. doi:10.1103/PhysRevLett.84.670

Clark, E. L., Krushelnick, K., Zepf, M., Beg, F. N., Tatarakis, M., Machacek, A., et al. (2000b). Energetic heavy-ion and proton generation from ultraintense laser-plasma interactions with solids. *Phys. Rev. Lett.* 85, 1654–1657. doi:10.1103/PhysRevLett.85.1654

Daido, H., Nishiuchi, M., and Pirozhkov, A. S. (2012). Review of laser-driven ion sources and their applications. *Reports on Progress in Physics* 75, 56401. doi:10.1088/0034-4885/75/5/056401

Datta, N. R., Rogers, S., and Bodis, S. (2019). Challenges and Opportunities to Realize "The 2030 Agenda for Sustainable Development" by the United Nations: Implications for Radiation Therapy Infrastructure in Low- and Middle-Income Countries. *International Journal of Radiation Oncology*Biology*Physics* 105, 918–933. doi:https://doi.org/10.1016/j.ijrobp.2019.04.033

De Loos, M. J. and Van der Geer, S. B. (1996). General Particle Tracer: A New 3D Code for Accelerator and Beamline Design

deGrassie, J. S. and Malmberg, J. H. (1980). Waves and transport in the pure electron plasma. *The Physics of Fluids* 23, 63–81. doi:10.1063/1.862864

Doria, D., Kakolee, K. F., Kar, S., Litt, S. K., Fiorini, F., Ahmed, H., et al. (2012). Biological effectiveness on live cells of laser driven protons at dose rates exceeding 10^9 Gy/s. *AIP Advances* 2, 011209. doi:10.1063/1.3699063

Dover, N., Nishiuchi, M., Sakaki, H., Kondo, K., Lowe, H., Alkhimova, M., et al. (2020). Demonstration of repetitive energetic proton generation by ultra-intense laser interaction with a tape target. *High Energy Density Physics* 37, 100847. doi:10.1016/j.hedp.2020.100847

Durante, M., Bräuer-Krisch, E., and Hill, M. (2018). Faster and safer? flash ultra-high dose rate in radiotherapy. *The British Journal of Radiology* 91, 20170628. doi:10.1259/bjr.20170628. PMID: 29172684

Favaudon, V., Caplier, L., Monceau, V., Pouzoulet, F., Sayarath, M., Fouillade, C., et al. (2014). Ultrahigh dose-rate flash irradiation increases the differential response between normal and tumor tissue in mice. *Science Translational Medicine* 6, 245ra93–245ra93. doi:10.1126/scitranslmed.3008973

Fiorini, F., Kirby, D., Borghesi, M., Doria, D., Jeynes, J. C., Kakolee, K. F., et al. (2011). Dosimetry and spectral analysis of a radiobiological experiment using laser-driven proton beams. *Phys Med Biol* 56,

6969–6982

Fitzmaurice, C., Akinyemiju, T. F., Al Lami, F. H., Alam, T., Alizadeh-Navaei, R., Allen, C., et al. (2018). Global, Regional, and National Cancer Incidence, Mortality, Years of Life Lost, Years Lived With Disability, and Disability-Adjusted Life-Years for 29 Cancer Groups, 1990 to 2016. *JAMA Oncology* 4, 1553. doi:10.1001/jamaoncol.2018.2706

Fourkal, E., Li, J. S., Ding, M., Tajima, T., and Ma, C. M. (2003). Particle selection for laser-accelerated proton therapy feasibility study. *Medical Physics* 30, 1660–1670. doi:10.1118/1.1586268

Fourrier, J., Martinache, F., Meot, F., and Pasternak, J. (2008). Spiral ffag lattice design tools. application to 6-d tracking in a proton-therapy class lattice. *Nucl. Instrum. Meth.* A589, 133–142. doi:10.1016/j.nima.2008.01.082

Gabor, D. (1947). A Space-Charge Lens for the Focusing of Ion Beams. *Nature* 160, 89–90. doi:10.1038/160089b0

Gauthier, M., Curry, C. B., Göde, S., Brack, F.-E., Kim, J. B., MacDonald, M. J., et al. (2017). High repetition rate, multi-mev proton source from cryogenic hydrogen jets. *Applied Physics Letters* 111, 114102. doi:10.1063/1.4990487

[Dataset] GmbH, P.-F. P.-T. W. D. P. (2019/2020). Ionizing radiation detectors. `https://www.ptwdosimetry.com/fileadmin/user_upload/DETECTORS_Cat_en_16522900_12/blaetterkatalog/blaetterkatalog/pdf/complete.pdf`. Accessed: 2020-09-23

González, W. and Prezado, Y. (2018). Spatial fractionation of the dose in heavy ions therapy: An optimization study. *Medical Physics* 45, 2620–2627. doi:10.1002/mp.12902

Grote, H. and Schmidt, F. (2003). MAD-X: An upgrade from MAD8. *Conf. Proc. C* 030512, 3497

Karger, C. P. and Peschke, P. (2017). RBE and related modeling in carbon-ion therapy. *Physics in Medicine & Biology* 63, 01TR02. doi:10.1088/1361-6560/aa9102

Kraft, S. D., Richter, C., Zeil, K., Baumann, M., Beyreuther, E., Bock, S., et al. (2010). Dose-dependent biological damage of tumour cells by laser-accelerated proton beams. *New Journal of Physics* 12, 85003. doi:10.1088/1367-2630/12/8/085003

Krest, D., Laslett, L., Jones, L. W., Symon, K., and Terwilliger, K. (1956). *Fixed field alternating gradient particle accelerators*. Tech. Rep. MURA-109, MURA-DWK-KRS-LJL-LWJ-KMT-3, Midwestern Universities Research Association (MURA), Madison, WI, USA

Kurup, A. (2019). Diagnostics for LhARA. *Low energy ion beam diagnostics workshop, Imperial College*

Lagrange, J. B., Appleby, R. B., Garland, J. M., Pasternak, J., and Tygier, S. (2018). Racetrack FFAG muon decay ring for nuSTORM with triplet focusing. *JINST* 13, P09013. doi:10.1088/1748-0221/13/09/P09013

Ledingham, K. W. D., McKenna, P., and Singhal, R. P. (2003). Applications for nuclear phenomena generated by ultra-intense lasers. *Science* 300, 1107–1111. doi:10.1126/science.1080552

Loeffler, J. S. and Durante, M. (2013). Charged particle therapy—optimization, challenges and future directions. *Nature Reviews Clinical Oncology* 10, 411–424. doi:10.1038/nrclinonc.2013.79

Malka, V., Fritzler, S., Lefebvre, E., d'Humières, E., Ferrand, R., Grillon, G., et al. (2004). Practicability of proton therapy using compact laser systems. *Medical Physics* 31, 1587–1592. doi:10.1118/1.1747751

Malmberg, J. H., Driscoll, C. F., Beck, B., Eggleston, D. L., Fajans, J., Fine, K., et al. (1988). Experiments with pure electron plasmas. *AIP Conference Proceedings* 175, 28–74. doi:10.1063/1.37613

Manti, L., Perozziello, F. M., Borghesi, M., Candiano, G., Chaudhary, P., Cirrone, G. A., et al. (2017). The radiobiology of laser-driven particle beams: Focus on sub-lethal responses of normal human cells. *Journal of Instrumentation* 12. doi:10.1088/1748-0221/12/03/C03084

Margarone, D., Cirrone, G. A. P., Cuttone, G., Amico, A., Andò, L., Borghesi, M., et al. (2018). Elimaia: A laser–driven ion accelerator for multidisciplinary applications. *Quantum Beam Science* 2. doi:10.3390/qubs2020008

Margarone, D., Velyhan, A., Dostal, J., Ullschmied, J., Perin, J. P., Chatain, D., et al. (2016). Proton acceleration driven by a nanosecond laser from a cryogenic thin solid-hydrogen ribbon. *Phys. Rev. X* 6, 041030. doi:10.1103/PhysRevX.6.041030

Martínez-Rovira, I., W, G., S, B., and Y, P. (2017). Carbon and oxygen minibeam radiation therapy: An experimental dosimetric evaluation. *Medical physics* 44. doi:10.1002/MP.12383

Masood, U., Bussmann, M., Cowan, T. E., Enghardt, W., Karsch, L., Kroll, F., et al. (2014). A compact solution for ion beam therapy with laser accelerated protons. *Applied Physics B* 117, 41–52. doi:https://doi.org/10.1007/s00340-014-5796-z

Masood, U., Cowan, T. E., Enghardt, W., Hofmann, K. M., Karsch, L., Kroll, F., et al. (2017). A light-weight compact proton gantry design with a novel dose delivery system for broad-energetic laser-accelerated beams. *Physics in Medicine & Biology* 62, 5531–5555. doi:10.1088/1361-6560/aa7124

Meusel, O., Droba, M., Glaeser, B., and Schulte, K. (2013). Experimental studies of stable confined electron clouds using Gabor lenses. *Conf. Proc. C* 1206051, 157–160. doi:10.5170/CERN-2013-002.157

Milluzzo, G. et al. (2017). Laser-accelerated ion beam diagnostics with TOF detectors for the ELIMED beam line. *JINST* 12, C02025. doi:10.1088/1748-0221/12/02/C02025

Milluzzo, G. et al. (2018). Geant4 simulation of the ELIMED transport and dosimetry beam line for high-energy laser-driven ion beam multidisciplinary applications. *Nucl. Instrum. Meth. A* 909, 298–302. doi:10.1016/j.nima.2018.02.066

Morrison, J. T., Feister, S., Frische, K. D., Austin, D. R., Ngirmang, G. K., Murphy, N. R., et al. (2018). MeV proton acceleration at kHz repetition rate from ultra-intense laser liquid interaction. *New Journal of Physics* 20, 22001. doi:10.1088/1367-2630/aaa8d1

Nevay, L. J. et al. (2020). Bdsim: An accelerator tracking code with particle-matter interactions. *Computer Physics Communications* , 107200

NIST (2017). *NIST Standard Reference Database 124* (Gaithersburg, MD, USA: National Institute of Standards and Technology). doi:https://dx.doi.org/10.18434/T4NC7P

Noaman-ul Haq, M., Ahmed, H., Sokollik, T., Yu, L., Liu, Z., Yuan, X., et al. (2017). Statistical analysis of laser driven protons using a high-repetition-rate tape drive target system. *Phys. Rev. Accel. Beams* 20, 041301. doi:10.1103/PhysRevAccelBeams.20.041301

Obst, L., Göde, S., Rehwald, M., Brack, F.-E., Branco, J., Bock, S., et al. (2017). Efficient laser-driven proton acceleration from cylindrical and planar cryogenic hydrogen jets. *Scientific Reports* 7, 10248. doi:10.1038/s41598-017-10589-3

Paganetti, H. (2014). Relative biological effectiveness (RBE) values for proton beam therapy. Variations as a function of biological endpoint, dose, and linear energy transfer. *Phys. Med. Biol.* 59, R419

Paganetti, H. and van Luijk, P. (2013). Biological considerations when comparing proton therapy with photon therapy. *Seminars in Radiation Oncology* 23, 77 – 87. doi:https://doi.org/10.1016/j.semradonc.2012.11.002. Controversies in Proton Therapy

Passoni, M., Bertagna, L., and Zani, A. (2010). Target normal sheath acceleration: theory, comparison with experiments and future perspectives. *New Journal of Physics* 12, 045012. doi:10.1088/1367-2630/12/4/045012

Pipek, J. et al. (2017). Monte Carlo simulation of the ELIMED beamline using Geant4. *JINST* 12, C03027. doi:10.1088/1748-0221/12/03/C03027

928 Planche, T., Fourrier, J., Lancelot, J. L., Meot, F., Neuveglise, D., and Pasternak, J. (2009). Design of a
929 prototype gap shaping spiral dipole for a variable energy protontherapy FFAG. *Nucl. Instrum. Meth.*
930 A604, 435–442. doi:10.1016/j.nima.2009.02.026
931 Pommarel, L., Vauzour, B., Mégnin-Chanet, F., Bayart, E., Delmas, O., Goudjil, F., et al. (2017). Spectral
932 and spatial shaping of a laser-produced ion beam for radiation-biology experiments. *Physical Review*
933 *Accelerators and Beams* 20, 1–10. doi:10.1103/PhysRevAccelBeams.20.032801
934 Pozimski, J. and Aslaninejad, M. (2013). Gabor lenses for capture and energy selection of laser driven ion
935 beams in cancer treatment. *Laser and Particle Beams* 31, 723—-733. doi:10.1017/S0263034613000761
936 Prezado, Y., Dos Santos, M., Gonzalez, W., Jouvion, G., Guardiola, C., Heinrich, S., et al. (2017a). Transfer
937 of Minibeam Radiation Therapy into a cost-effective equipment for radiobiological studies: a proof of
938 concept. *Scientific Reports* 7, 17295. doi:10.1038/s41598-017-17543-3
939 Prezado, Y. and Fois, G. (2013). Proton-minibeam radiation therapy: a proof of concept. *Medical physics*
940 40. doi:10.1118/1.4791648
941 Prezado, Y., Jouvion, G., Hardy, D., Patriarca, A., Nauraye, C., Bergs, J., et al. (2017b). Proton minibeam
942 radiation therapy spares normal rat brain: Long-Term Clinical, Radiological and Histopathological
943 Analysis. *Scientific Reports* 7, 14403. doi:10.1038/s41598-017-14786-y
944 Prezado, Y., Jouvion, G., Patriarca, A., Nauraye, C., Guardiola, C., Juchaux, M., et al. (2018). Proton
945 minibeam radiation therapy widens the therapeutic index for high-grade gliomas. *Scientific Reports* 8.
946 doi:10.1038/s41598-018-34796-8
947 [Dataset] PTCOG (2020). Particle Therapy Co-Operative Group
948 PTW (2009). *User Manual Water Phantom T41023*. PTW-Freiburg Physikalisch-Technische Werkstatten
949 Dr. Pychlau GmbH, Freiburg, Germany, d738.131.00/02 en edn.
950 Reiser, M. (1989). Comparison of gabor lens, gas focusing, and electrostatic quadrupole focusing for
951 low-energy ion beams. In *Proceedings of the 1989 IEEE Particle Accelerator Conference, . 'Accelerator*
952 *Science and Technology* (Chicago, IL, USA), 1744–1747 vol.3
953 Romano, F., Schillaci, F., Cirrone, G., Cuttone, G., Scuderi, V., Allegra, L., et al. (2016a). The elimed
954 transport and dosimetry beamline for laser-driven ion beams. *Nuclear Instruments and Methods in*
955 *Physics Research Section A: Accelerators, Spectrometers, Detectors and Associated Equipment* 829,
956 153–158. doi:https://doi.org/10.1016/j.nima.2016.01.064. 2nd European Advanced Accelerator Concepts
957 Workshop – EAAC 2015
958 Romano, F. et al. (2016b). The ELIMED transport and dosimetry beamline for laser-driven ion beams.
959 *Nucl. Instrum. Meth. A* 829, 153–158. doi:10.1016/j.nima.2016.01.064
960 Roth, M. and Schollmeier, M. (2016). Ion Acceleration - Target Normal Sheath Acceleration. In *CAS*
961 *- CERN Accelerator School: Plasma Wake Acceleration* (Geneva: CERN), 231–270. doi:10.5170/
962 CERN-2016-001.231
963 Schillaci, F. et al. (2019). Advanced Beam Transport Solutions for ELIMAIA: A User Oriented Laser-
964 Driven Ion Beamlines. In *10th International Particle Accelerator Conference* (Melbourne, Australia),
965 TUPTS005. doi:10.18429/JACoW-IPAC2019-TUPTS005
966 Snavely, R. A., Key, M. H., Hatchett, S. P., Cowan, T. E., Roth, M., Phillips, T. W., et al. (2000). Intense
967 high-energy proton beams from petawatt-laser irradiation of solids. *Phys. Rev. Lett.* 85, 2945–2948.
968 doi:10.1103/PhysRevLett.85.2945
969 Symon, K. R., Kerst, D. W., Jones, L. W., Laslett, L. J., and Terwilliger, K. M. (1956). Fixed-field
970 alternating-gradient particle accelerators. *Phys. Rev.* 103, 1837–1859. doi:10.1103/PhysRev.103.1837
971 Tanigaki, M., Mori, Y., Inoue, M., Mishima, K., Shiroya, S., Ishi, Y., et al. (2006). Present status of the
972 ffag accelerators in kurri for ads study. In *EPAC 2006 - Contributions to the Proceedings* (Edinburgh,

Untied Kingdom)
[Dataset] TECH-X (2020). Vsim for plasma. https://www.txcorp.com/vsim
[Dataset] The EPICS collaboration (2020). The Experimental Physics and Industrial Control System. https://epics-controls.org
The LhARA consortium (2020). *The Laser-hybrid Accelerator for Radiobiological Applications*. Tech. Rep. CCAP-TN-01, The Centre for the Clinical Application of Particles, Imperial College London. https://ccap.hep.ph.ic.ac.uk/trac/raw-attachment/wiki/Communication/Notes/CCAP-TN-01.pdf
[Dataset] The World Health Organisation (2020). Cancer. https://www.who.int/news-room/fact-sheets/detail/cancer
Thompson, R. C. (2015). PENNING TRAPS. In *Trapped Charged Particles* (WORLD SCIENTIFIC (EUROPE)), Advanced Textbooks in Physics. 1–33. doi:doi:10.1142/9781786340139_0001
Tsoupas, N. et al. (1991). Uniform beam distributions using octupoles. *Proceedings of PAC 1991* , 1695–1697
Uesugi, T. (2018). Betatron Tune Measurement . *FFA School, Osaka*
Urakabe, E. et al. (1999). Beam-profile control using an octupole magnet. *Jpn. J. Appl. Phys.* 38, 6145–6149
Vitti, E. T. and Parsons, J. L. (2019). The radiobiological effects of proton beam therapy: Impact on dna damage and repair. *Cancers* 11. doi:10.3390/cancers11070946
Vozenin, M.-C., Hendry, J. H., and Limoli, C. L. (2019). Biological benefits of ultra-high dose rate flash radiotherapy: Sleeping beauty awoken. *Clinical Oncology* 31, 407–415. doi:10.1016/j.clon.2019.04.001
Wang, H. (2014). Wavefront measurement techniques used in high power lasers. *High Power Laser Science and Engineering* 2
Wiggins, S. M., Boyd, M., Brunetti, E., Butler, N. M. H., Feehan, J. S., Gray, R. J., et al. (2019). Application programmes at the Scottish Centre for the Application of Plasma-based Accelerators (SCAPA). In *Relativistic Plasma Waves and Particle Beams as Coherent and Incoherent Radiation Sources III*, eds. D. A. Jaroszynski and M. Hur. International Society for Optics and Photonics (Prague, Czech Republic: SPIE), vol. 11036, 93 – 103. doi:10.1117/12.2520717
Wilkens, J. J. and Oelfke, U. (2004). A phenomenological model for the relative biological effectiveness in therapeutic proton beams. *Physics in Medicine and Biology* 49, 2811–2825. doi:10.1088/0031-9155/49/13/004
Willingale, L., Nagel, S. R., Thomas, A. G. R., Bellei, C., Clarke, R. J., Dangor, A. E., et al. (2009). Characterization of High-Intensity Laser Propagation in the Relativistic Transparent Regime through Measurements of Energetic Proton Beams. *Physical Review Letters* 102, 125002. doi:10.1103/PhysRevLett.102.125002
Wilson, J., Hammond, E. M., Higgins, G. S., and Petersson, K. (2020a). Corrigendum: Ultra-High Dose Rate (FLASH) Radiotherapy: Silver Bullet or Fool's Gold? *Frontiers in Oncology* 10, 210. doi:10.3389/fonc.2020.00210
Wilson, J. D., Hammond, E. M., Higgins, G. S., and Petersson, K. (2020b). Ultra-high dose rate (flash) radiotherapy: Silver bullet or fool's gold? *Frontiers in Oncology* 9, 1563. doi:10.3389/fonc.2019.01563
Yogo, A., Maeda, T., Hori, T., Sakaki, H., Ogura, K., Nishiuchi, M., et al. (2011). Measurement of relative biological effectiveness of protons in human cancer cells using a laser-driven quasimonoenergetic proton beamline. *Applied Physics Letters* 98, 053701. doi:10.1063/1.3551623
Yonemura, Y., Arima, H., Ikeda, N., Ishibashi, K., Maehata, K., Noro, T., et al. (2008). Status of center for accelerator and beam applied science of kyushu university. *EPAC 2008 - Contributions to the*

Proceedings

Zeil, K., Baumann, M., Beyreuther, E., Burris-Mog, T., Cowan, T. E., Enghardt, W., et al. (2013). Dose-controlled irradiation of cancer cells with laser-accelerated proton pulses. *Applied Physics B* 110, 437–444. doi:10.1007/s00340-012-5275-3

Zlobinskaya, O., Siebenwirth, C., Greubel, C., Hable, V., Hertenberger, R., Humble, N., et al. (2014). The effects of ultra–high dose rate proton irradiation on growth delay in the treatment of human tumor xenografts in nude mice. *Radiation Research* 181, 177–183. doi:10.1667/RR13464.1